Study of W^+W^--Production with the ATLAS Detector at the LHC

Untersuchung der W^+W^--Produktion mit dem ATLAS Detektor am LHC

Masterarbeit an der Fakultät für Physik
der
Ludwig-Maximilians-Universität München

vorgelegt von
Florian Rättich
geboren am 17. Januar 1986 in Memmingen

27. April 2013

Gutachterin: Prof. Dr. Dorothee Schaile

Abstract

This thesis presents studies of the W^+W^- production with the ATLAS detector at the LHC. The data used was recorded during the year 2012 and corresponds to an integrated luminosity of $20.1\,\mathrm{fb}^{-1}$. This analysis is focused on the dileptonic decay channel of the dibosons. The background due to $Z \to \tau\tau$ production is investigated and possible optimizations to suppress this background are studied. The background from cosmic muons is estimated. Results from this thesis contribute to an official ATLAS measurement of the W^+W^- production cross section, which is in preparation as a conference contribution.

Zusammenfassung

In dieser Arbeit wird die Produktion von W^+W^- Bosonpaaren mit dem ATLAS Detektor am LHC untersucht. Dazu werden Daten verwendet, die einer integrierten Luminosität von $20.1\,\mathrm{fb}^{-1}$ entsprechen. Die Analyse konzentriert sich auf den leptonischen Zerfallskanal der W^+W^- Paare. Der von $Z \to \tau\tau$ Zerfällen stammende Untergrund wird untersucht. Dabei werden mögliche Optimierungen, die diesen Untergrund unterdrücken, systematisch untersucht. Desweiteren wird der Untergrund durch kosmische Myonen bestimmt. Ergebnisse dieser Arbeit tragen zu einer offiziellen ATLAS Messung des Wirkungsquerschnitts für die Produktion eines W^+W^- Bosonpaares am LHC mit dem ATLAS Detektor bei, die allerdings noch nicht komplett abgeschlossen ist.

Contents

1 Introduction

The Standard Model (SM) of particle physics was developed during the middle of the 20th century. It describes the smallest constituents of matter and their interactions by the strong, electromagnetic, and the electroweak forces. These forces are mediated by the 12 gauge bosons. However, it could not explain the experimentally observed masses of the electroweak W and Z bosons. In 1964 Robert Brout, Francois Englert, and Peter Higgs, formulated a mechanism which was able to explain the masses of the bosons [1]. This mechanism introduced a new field to the SM which conserves its global gauge symmetry. In addition this mechanism predicts a massive spin 0 particle, the Higgs boson.

The Large Hadron Collider is a synchrotron proton-proton collider with a design center of mass energy of $\sqrt{s} = 14\,\text{TeV}$. The two largest experiments at the LHC are the ATLAS and the CMS detector. In August 2012 evidence of a new boson was found at the ATLAS [2] and at the CMS experiment [3], at a mass of 125 GeV. On March 14th 2013, CERN confirmed that the discovered boson is a Higgs boson [4]. The first mass measurement was updated in the year 2013 using up to $25\,\text{fb}^{-1}$ of proton proton collision data. The result of this measurement is a Higgs boson mass of $125.5 \pm 0.2\,(\text{stat})^{+0.5}_{-0.6}\,(\text{syst})\,\text{GeV}$.

This measurement includes the decay of Higgs boson into W^+W^- pairs. The W^+W^- pair production process is one irreducible background in the channel of the $H \to W^+W^-$ decay. For precise results it is therefore important to accurately measure the production cross section of W^+W^- pairs.

Additionally, a comparison of the measured W^+W^- production cross section with its theoretical prediction offers a test of the SM. Deviations between the predicted and the measured cross section could indicate new physics. The cross section of this process increases with the center of mass energy. Therefore the high center of mass energy at the LHC offers an opportunity to search for new physics.

In this analysis, the W^+W^- production at a center of mass energy of $\sqrt{s} = 8\,\text{TeV}$ in proton proton collisions at the LHC is studied. The full data recorded during 2012 at the ATLAS experiment is used. The contribution of the $Z \to \tau\tau$ decay is studied and a cut optimization study is presented. The cosmic muon background is estimated.

2 | Theoretical Background

2.1 The Standard Model

The SM is a theory that describes the interactions of particle physics very well. It was first formulated in the middle of the 20th century. The experimental confirmation of the existence of quarks, like the discovery of the bottom quark in 1977 [5] and the discovery of the top quark at TeVatron in 1995 [6], was a very important supporting evidence of the SM.

In the SM, the smallest constituents of matter are three generations of fermions. These particles and their properties are listed in table 2.1. Each generation has color charged up- and down-type quarks, an electrically charged lepton, and a neutral lepton-neutrino. Every fermion has its own anti-particle, with opposite sign and opposite parity [7].

Interactions are described via the basic forces, the electromagnetic, the weak, and the strong force. The electromagnetic force is responsible for phenomenas such as light, magnetism or electricity, and is described by the theory of Quantum Electrodynamics (QED). The massless photon acts as mediator for the electromagnetic force. The weak force, which is for example responsible for radioactive decay of particles like the β-decay, is mediated by massive $W^{\pm}$ and Z boson, and is described in the theory of Quantum Flavordynamics (QFD). The electromagnetic and weak force are described together by the Electroweak Theory (EW). The strong force has eight dicolored carriers named gluons and it is responsible for the bindings of quarks to hadrons. The theory of the strong force is Quantum Chromodynamics (QCD). The Higgs mechanism, which explains the mass of the electroweak gauge bosons, predicts a further boson, the Higgs boson. The mass of the Higgs boson was measured at $125.5 \pm 0.2\,(\text{stat})^{+0.5}_{-0.6}\,(\text{syst})\,\text{GeV}$ [8]. Table 2.2 lists the charge and the mass, of the bosons mentioned above.

Generation	Fermion	Flavor	Charge [e]	Mass	
1st	up quark	u	$+\frac{2}{3}$	$2.3^{+0.7}_{-0.5}$	MeV
	down quark	d	$-\frac{1}{3}$	$4.8^{+0.7}_{-0.3}$	MeV
	electron	e	-1	0.511	MeV
	electron-neutrino	ν_e	0	< 2	eV
2nd	charm quark	c	$+\frac{2}{3}$	1.275 ± 0.025	GeV
	strange quark	s	$-\frac{1}{3}$	95 ± 5	MeV
	muon	μ	-1	105.7	MeV
	muon-neutrino	ν_μ	0	< 0.19	eV
3rd	top quark	t	$+\frac{2}{3}$	$173.5 \pm 0.6 \pm 0.8$	GeV
	bottom quark	b	$-\frac{1}{3}$	4.18 ± 0.03	GeV
	tau	τ	-1	1776.82 ± 0.16	MeV
	tau-neutrino	ν_τ	0	< 18.2	MeV

Table 2.1: Fermions of the SM and their basic properties [9].

Boson	Force	Charge [e]	Mass	
Higgs H		0	$125.5 \pm 0.2\,^{+0.5}_{-0.6}$	GeV
photon γ	electromagnetic	0	$< 1 \cdot 10^{-18}$	eV
Z	electroweak	0	91.1876 ± 0.0021	GeV
$W^\pm$	electroweak	± 1	80.385 ± 0.015	GeV
gluon g	strong	0	0	eV

Table 2.2: Gauge-bosons of the SM [9].

2.2 Lagrangian Formalism in the Standard Model

Dynamics of a physical system can be described by the Lagrangian density $\mathcal{L}$. In classical mechanics, the Lagrangian is constructed as the difference of the potential energy and the kinematic energy of a system. In field theory the Lagrangian is a function of fields, the derivatives of the fields and the spatial coordinates [10]. The Euler-Lagrange equation determines the dynamics of

the system and is defined as

$$\frac{\partial}{\partial x_\mu}\left(\frac{\partial \mathcal{L}}{\partial(\partial\phi/\partial x_\mu)}\right) - \frac{\partial \mathcal{L}}{\partial \phi} = 0. \tag{2.1}$$

Here ϕ are the fields and $\partial\phi/\partial x_\mu$ the derivatives of the fields with respect to the coordinates x_μ.

The complete Lagrangian density for the SM can be denoted as the summation of three terms, the QCD term, the EW term, and the Higgs term:

$$\mathcal{L} = \mathcal{L}_{QCD} + \mathcal{L}_{EW} + \mathcal{L}_{Higgs}. \tag{2.2}$$

The field theory describing the SM is a gauge field theory. In gauge theories, the Lagrangian is required to be invariant under a group of local transformations. The SM contains the inertial symmetries of the unitary product group $SU(3)_C \times SU(2)_L \times U(1)_Y$.

2.2.1 Quantum Chromodynamics

The QCD is invariant under transformation under the group of $SU(3)_C$. The local symmetry is defined by the color charge, given as the index C. The color charge is divided in three values, red, blue, and green. Color charged fermions, namely the quarks, are charged with one color. In contrast, the interaction boson of the strong force, the gluon, is charged with a color and an anticolor. Gluons are di-color charged. The symmetry group of the QCD is $SU(N)$. Therefore there are $N^2 - 1$ generators for this group. For the gluons this means, there are 6 different di-color charged gluons and two superpositions of same di-color charged gluons. In sum there are 8 gluons. However the force between two color-charged particles does not decrease when they are separated. The binding energy of the particles would rise to infinitely high values. This principle is called color confinement. This groups together to hadrons, where a pair of quark and antiquark combine to a meson, or three quarks combine to a baryon.

The QCD Lagrangian is defined as

$$\mathcal{L}_{QCD} = \sum_k i\bar{q}_k\gamma_\mu(D^\mu - ig_s G_a^\mu \frac{\lambda^a}{2})q_k - \frac{1}{4}G^a_{\mu\nu}G_a^{\mu\nu}, \tag{2.3}$$

where λ^a are the generators the symmetry group, q_k the fields describing the quarks and $\bar{q}_k$ for antiquark fields, γ_μ the Dirac matrices, and $G^a_{\mu\nu}$ the gluon field strength tensor. This tensor characterizes the interaction between gluons and quarks and is defined as

$$G^a_{\mu\nu} = \partial_\mu G^a_\nu - \partial_\nu G^a_\mu - g_s f_{abc} G^b_\mu G^c_\nu, \tag{2.4}$$

where g_s is given in terms of the strong coupling constant, as $g_s = \sqrt{4\pi\alpha_s}$. The last term of the QCD Lagrangian, given in equation 2.3 shows, that gluons can interact with each other.

2.2.2 Electroweak Theory

Central to the Electroweak Theory is the $SU(2)_L \times U(1)_Y$ symmetry [11]. The generator of $U(1)$ is the weak hypercharge Y, which is composed of the electrical charge Q and the third component of the weak isospin T_3. The hypercharge is defined as

$$Y = 2(Q - T_3). \tag{2.5}$$

T_3 is the generator of the $SU(2)$ symmetry group. This leads to four gauge fields, three denoted as W_μ^i where $i \in [1, 2, 3]$ and one named B_μ. The Lagrangian density for EW theory is given by

$$\mathcal{L}_{EW} = \sum_k i\bar{\psi}_k \gamma_\mu D^\mu \psi_k - \frac{1}{4} F_{\mu\nu} F^{\nu\mu} - \frac{1}{4} B_{\mu\nu} B^{\nu\mu}. \tag{2.6}$$

Similarly to the Lagrangian of QCD, as written down in equation 2.3, where the fermions are described by q_i, fermions in the EW Lagrangian are denoted as ψ_k. The field strength tensor of the EW and covariant derivatives are defined as:

$$F_{\mu\nu}^j = \partial_\mu W_\nu - \partial_\nu W_\mu - g W_\mu \times W_\nu, \tag{2.7}$$

$$D_\mu = \partial_\mu - ig\frac{\tau}{2} W_\mu - ig'\frac{Y}{2} B_\mu, \tag{2.8}$$

$$B_{\mu\nu} = \partial_\mu B_\nu - \partial_\nu B_\mu. \tag{2.9}$$

The fields W_μ^i and B_μ need to be massless gauge fields to preserve the symmetry, the observable states of these fields can gain mass via spontaneous symmetry breaking. The mass eigenstates of the $\mathcal{L}_{EW}$ are:

$$A_\mu = B_\mu \cos\theta_W + W_\mu^3 \sin\theta_W, \tag{2.10}$$

$$Z_\mu = -B_\mu \sin\theta_W + W_\mu^3 \cos\theta_W, \tag{2.11}$$

$$W_\mu^\pm = \frac{1}{\sqrt{2}} \left(W_\mu^1 \mp i W_\mu^2 \right). \tag{2.12}$$

Here $W_\mu^\pm$ corresponds to the electrical charged W boson, and Z_μ to the neutral Z boson, depending on the Weinberg angle θ_W. The term A_μ describes the photon, which remains massless.

2.2.3 The BEH Mechanism

The underlying electroweak fields are massless, since terms with mass would break the gauge symmetry. However, it can be observed that some electroweak gauge bosons, namely the $W^{\pm}$ and Z^0, are massive. This can be explained by introducing a new complex scalar field, the Higgs field. This is known as the Brout-Englert-Higgs [12][13][1] (or Higgs) mechanism, which explains the mass of the bosons via electroweak symmetry breaking. Therefore the Lagrangian for the BEH mechanism is given by

$$\mathcal{L}_{Higgs} = |D_\mu \phi|^2 - V(\phi) - \sum_j c_j \bar{q}_j \phi_j q_j - \sum_k f_k \bar{\psi}_k \phi \psi_k. \tag{2.13}$$

The scalar field ϕ is defined as

$$\phi = \begin{pmatrix} \phi^+ \\ \phi^0 \end{pmatrix}. \tag{2.14}$$

The potential of the field is given by

$$V\left(\phi^\dagger \phi\right) = \mu^2 \phi^\dagger \phi - \lambda \left(\phi^\dagger \phi\right)^2. \tag{2.15}$$

Minimizing the potential in respect of $\mu^2 < 0$ leads to the "Mexican hat" potential, which is depicted in figure 2.1. The minimum is not located at $\phi = 0$, instead it is around the finite value $\pm\nu$. This values is known as the vacuum expectation value of the Higgs potential and is given by $\nu = \sqrt{-\mu^2/\lambda}$. By expanding the Lagrangian around this minimum one can obtain the mass eigenstates as denoted in section 2.2.2. The masses of fermions can be explained via Yukawa coupling to the Higgs field and is described by the last term of the Higgs Lagrangian. Furthermore the mechanism predicts a massive boson, the Higgs boson which can be seen as an excitation of the Higgs field.

2.3 Proton-Proton Collisions at the LHC

One important quantity for characterizing an accelerator is the energy with which the accelerated particles collide. This is important since some kinematically processes are not possible with a low center of mass energy. The center of mass energy is given as the square root of the Mandelstam variable:

$$s = (\vec{p}_1 + \vec{p}_2)^2. \tag{2.16}$$

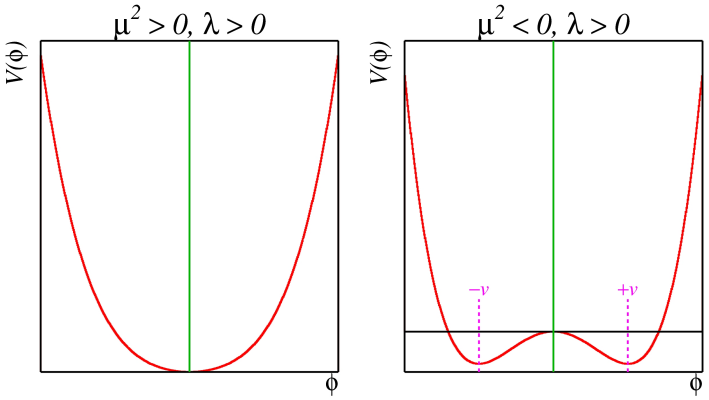

Figure 2.1: The complex scalar Higgs potential. On the left for $\mu^2 > 0$, $\lambda > 0$ on the right with the minima around the vacuum expectation values $\pm\nu$ in case of $\mu^2 < 0$, $\lambda > 0$ [14].

The four momenta of the accelerated particles are denoted as $\vec{p}_1$ and $\vec{p}_2$. In case of particles with same mass and same energy E_i, the center of mass energy simplifies to $\sqrt{s} = 2E_i$.

Another important variable in collision at high energy experiments is the integrated luminosity $\mathcal{L}$. The integrated luminosity describes the rate of collisions over a period of time. One can calculate the number of events N by multiplying the integrated luminosity with the cross section of the process: $N = \sigma\mathcal{L}$. At storage rings, the luminosity can be calculated by

$$\mathcal{L} = \frac{fnN_1N_2}{A}. \tag{2.17}$$

where f is the circulation frequency of the proton bunches, n the number of proton bunches circulating the storage ring, and N_i the number of protons in the actual bunch. The cross section A can be rewritten as

$$A = 4\pi\sigma_x\sigma_y \tag{2.18}$$

under the assumption of a Gaussian density distribution of the beam in x and y direction [15].

2.3.1 W^+W^- Production

In proton-proton collisions the W^+W^- boson pair is produced via quark or gluon initial states. The dominant leading order process has a quark and an

anti-quark in initial state, decaying into a W diboson pair exchanging a third virtual anti-quark. This process is called "t-channel". One further process is the annihilation of a quark and anti-quark to $Z^0/\gamma*$ which decays into the W^+W^- diboson pair. This process happens via the triple gauge boson interaction vertex. Both processes are depicted in figure 2.2.

One non-negligible next-to-leading order (NLO) production mechanism has two gluons in the initial state, decaying into the W^+W^- diboson pair via a fermion box. The contribution of this process to the overall production cross-section is about $\approx 3\%$ and is shown in figure 2.3.

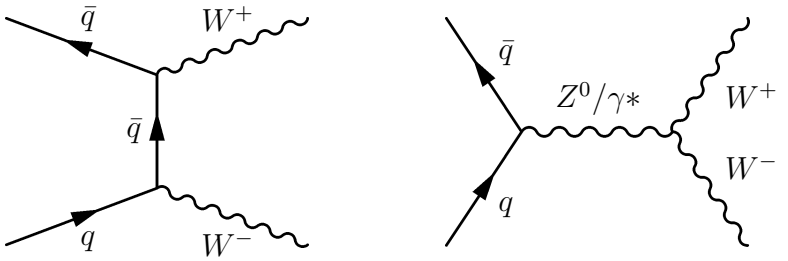

(a) t-channel (b) s-channel

Figure 2.2: Feynman tree level graphs for W^+W^- production mechanism at leading order, with quark initial states.

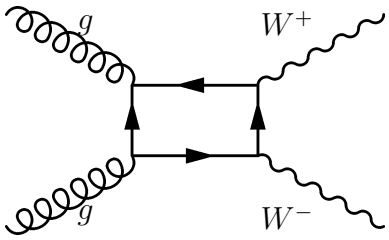

Figure 2.3: NLO Feynman diagram of gluon initial state with a fermion box.

In nuclear physics it is common practice to state cross sections in the unit of "barn". A "barn" is defined as $1\,b = 10^{-28}\,m^2$ which is in the magnitude of the cross section of a heavy nucleus. Therefore $1\,pb = 10^{-40}\,m^2$. In leading order the calculated production cross section for the W^+W^- diboson pair is 35.56 pb. The next-to-leading order production cross section for a center of mass energy of $\sqrt{s} = 8\,\text{TeV}$ is $57.22^{+4.1\%}_{-2.8\%}$ pb [16] as shown in table 2.3. According to the predicted cross section, the recorded data of $20.1\,\text{fb}^{-1}$ contains roughly 1.2 million W^+W^- diboson events.

$\sqrt{s}$ [TeV]	$\sigma^{LO}(W^+W^-)$ [pb]	$\sigma^{NLO}(W^+W^-)$ [pb]
7	29.51	$47.02^{+4.3\%}_{-3.2\%}$
8	35.56	$57.22^{+4.1\%}_{-2.8\%}$
13	67.74	$112.64^{+3.0\%}_{-2.3\%}$
14	74.48	$124.31^{+2.8\%}_{-2.0\%}$

Table 2.3: Total cross section of W^+W^- at the LHC for the different center of mass energies $\sqrt{s}$, in leading order (LO) and next-to-leading order (NLO) [16].

2.3.2 Background Processes

In the dilepton search for a W^+W^- boson pair, there is no strong background. However there are several backgrounds which are contributing to the final state. They will be explained in the following section.

Z+Jets
A background with a high contribution is the Drell-Yan process. In this case a Z or $\gamma*$ produced by quark-antiquark annihilation decays into two oppositely charged leptons, sometimes with associated jets. This process has a signature of two opposite charged same flavor leptons. Mismeasurements or τ decays can lead to apparently missing transverse energy. The invariant mass spectrum of the two leptons peak around 91.2 GeV which is the mass of the Z boson.

$t\bar{t}$ and Wt
The dominant top quark decay is $t \to W^+b$. When the W boson decays leptonically and no high energy jet is detected or the jet is mismeasured as a lepton, the resulting signature is signal-like. The leptons in the final state will be opposite charged since $t\bar{t}$ is it as well.

W+Jets
The production of a single $W^{\pm}$ boson with jets has a high cross section. When a jet is misidentified as a high energy lepton and the W boson decays into a lepton neutrino pair, the signature of this process is signal-like.

$W + \gamma$
The $W + \gamma$ background is similar to the W+Jets process. The γ can be misidentified as a lepton. Together with a lepton from W boson decay and the missing transverse energy from the neutrino, the event is in the signal region.

$WZ \to l\nu ll$
When a W decays into $l\nu$ and together with an $Z \to ll$ the final state of this process has three leptons and one neutrino. In case one lepton is mismeasured or not well reconstructed the event is signal-like. However the two leptons are not always oppositely charged, depending on mismeasured lepton.

$ZZ \to ll\nu\nu$
Z diboson events can decay into two oppositely charged leptons and two neutrinos where the invariant mass of the dilepton system is not near the Z mass. This event has the same signature as the dileptonic W^+W^- decay.

QCD
Multijet events can contribute as a background to the signal region. For this, two jets need to be misidentified as two leptons and cause a mismeasurement of the missing transverse energy which is very rare.

3 | Experimental Setup

3.1 The Large Hadron Collider

The LHC has a circumference of 26.7 km, making it the largest particle accelerator to date. It is a synchrotron proton-proton accelerator located at European Organization for Nuclear Research (CERN) and it is the successor of Large Electron Positron Collider (LEP). The tunnel in which the accelerator is built in is located between 45 m and 170 m below the surface. The LHC is designed for a center of mass energy of $\sqrt{s} = 14\,\text{TeV}$ and a luminosity of $10^{34}\,\text{cm}^{-2}\,\text{s}^{-1}$ TeV[17]. The LHC uses protons with an injection energy of 450 GeV. The pre-accelerators are called LINAC2, PS Booster, PS, and SPS. The whole accelerator chain is depicted in figure 3.1. During 2010 and 2011 the beam energy was limited to $E_i = 3.5\,\text{TeV}$, from 2012 to the beginning of 2013 the beam energy was at $E_i = 4\,\text{TeV}$ and delivered $\mathcal{L} = 23.3\,\text{fb}^{-1}$ of integrated luminosity [18]. After the technical upgrade the LHC will perform at the full beam energy of $E_i = 6.5\,\text{TeV}$ in 2015.

The proton beams are propagating in a beam pipe in a high vacuum of $10^{-8} - 10^{-9}$ Pa. The beams are kept on track by the 1232 superconducting dipole magnets, which are the biggest magnets among the about 9593 built-in magnets [20]. The dipole magnets are cooled down to a temperature of 1.9 K. The beams are focused so that they collide at four points of the ring, in the centre of the four largest experiments of the LHC. These four experiments are A Toroidal LHC Aparatus (ATLAS), Compact Muon Solenoid (CMS), A Large Ion Collider Experiment (ALICE) and Large Hadron Collider beauty (LHCb). While ALICE is designed to probe heavy ion collisions and LHCb is specialized to investigate the parameters of CP violation, ATLAS and CMS are high precision general purpose detectors. One main focus is the search for the Higgs boson and the investigation of its properties.

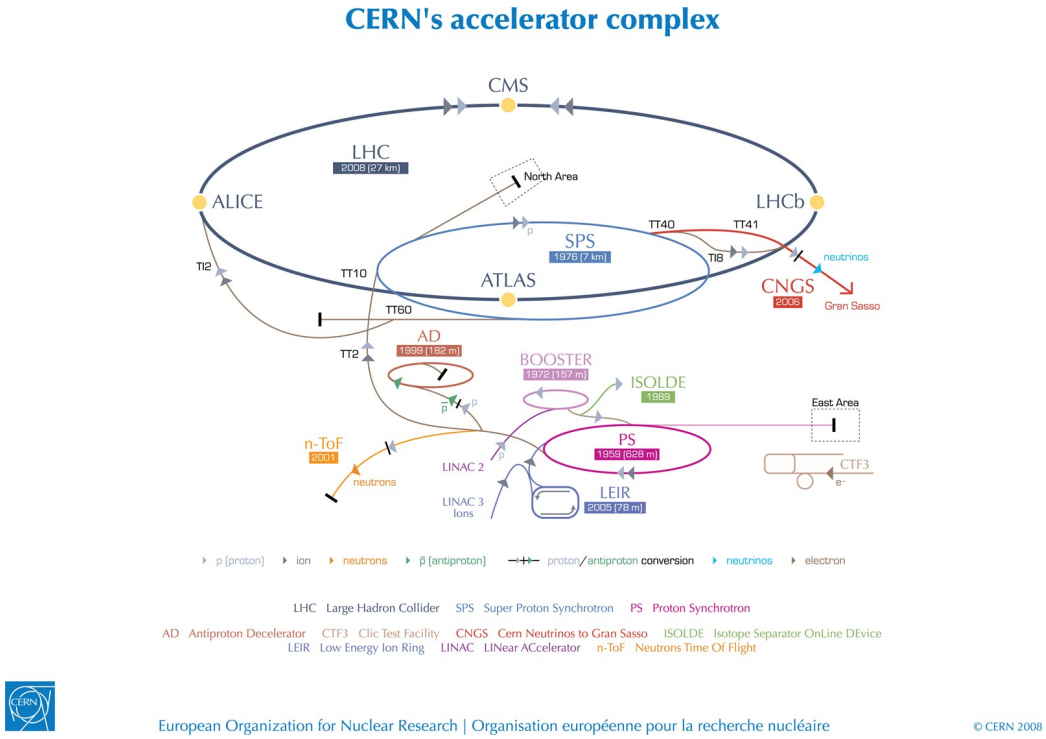

Figure 3.1: Overview of the CERN accelerators including the injector chain and the LHC [19].

3.2 The ATLAS Experiment

The ATLAS detector is the largest of the seven detectors located at the LHC. It is 46 m long and has a diameter of 25 m. The detector is located at LHC point 1 in a cavern 92 m below the surface. The ATLAS Collaboration consists of more than 3000 physicists from 175 institutions around the world, helping to analyze the data of $\mathcal{L} = 20.1\,\mathrm{fb}^{-1}$ which was recorded during the $\sqrt{s}$ =8 TeV run during 2012. The main parts of the detector are described in the following section. Figure 3.2 shows a computer generated picture of the whole ATLAS detector.

3.2.1 Coordinate System

The coordinate system used in the ATLAS experiment is a right-handed Cartesian coordinate system, which has its origin in the nominal interaction point. This is the point where the two beams are brought to collision and it is also the centre of the detector. The beam axis is parallel to the z-

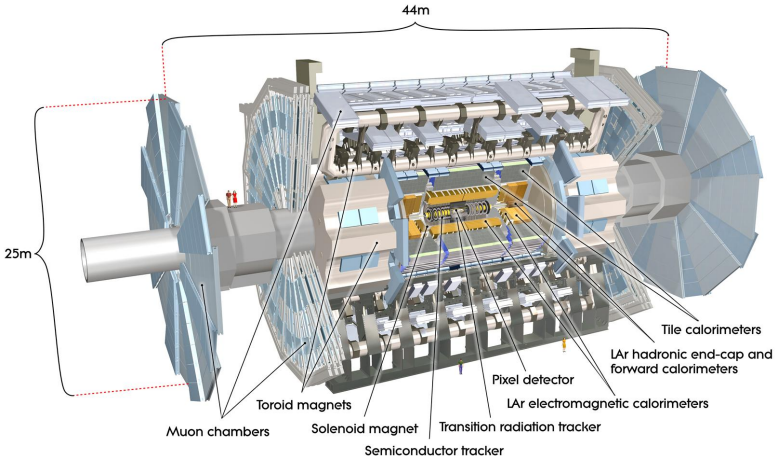

Figure 3.2: Schematic picture of the complete ATLAS detector [21].

axis, the x-axis points to the middle of the accelerator ring and the y-axis points upwards. Consequently the transverse plane is spanned by the x-y plane. Furthermore the transverse momentum or energy is the corresponding momentum or energy in the x-y plane. The transverse energy is calculated by

$$E_T = \sqrt{E_x^2 + E_y^2}. \tag{3.1}$$

The transverse momentum is calculated analogously by

$$p_T = \sqrt{p_x^2 + p_y^2}. \tag{3.2}$$

The azimuthal angle ϕ is defined in the transverse plane around the z-axis and the polar angle θ refers to the angle around the x-axis. Furthermore one can define the pseudorapidity, which describes the angle of a particle with respect to the beam axis. This parameter is defined as

$$\eta = -\ln \tan \theta/2. \tag{3.3}$$

From the definition follows that $\eta = 0$ for $\theta = 90\,^\circ$. For $\theta = 0^\circ$ or $\theta = 180^\circ$, the pseudorapidity approaches $\pm\infty$. The angular distance between two objects in this coordinate system is defined as

$$\Delta R = \sqrt{\Delta\phi^2 + \Delta\eta^2}, \tag{3.4}$$

describing the radius of a cone.

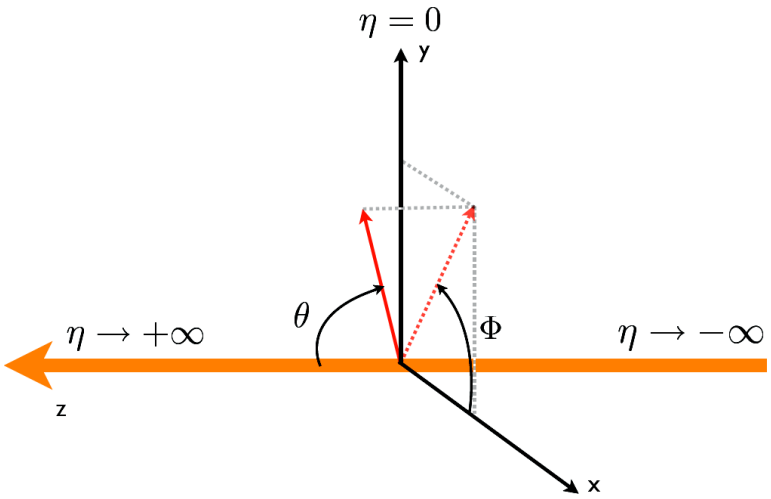

Figure 3.3: Coordinate system used at the ATLAS experiment. The z-axis is aligned parallel to the beam axis [22].

3.2.2 The Magnet System

The Lorentz force, which is given by

$$F_{\text{Lorentz}} = q \cdot (\vec{v} \times \vec{B}), \tag{3.5}$$

deflects charged particles, proportional to their momentum as they are propagating through a magnetic field. Measuring the curvature of the deflected particle is a common method to estimate the momentum of charged particles in particle detectors. At the ATLAS detector the magnetic field is generated by two types of magnet systems. There is one central solenoid with a size of 5.3 m length and a diameter of 2.4 m [23]. It generates a magnetic field of 2 T for the inner detector. The barrel toroid has a length of 25.3 m and an outer diameter of 20.1 m. With its eight symmetrically distributed coils around the axis, it provides a magnetic field of 4 T. Smaller separate toroids are placed in every endcap. They are 5 m long and have an outer diameter of 10.7 m. The working point temperature of the toroids is 4.7 K and they operate with a nominal current of 2.5 kA [23].

3.2.3 The Inner Detector

The Inner Detector (ID) is located straight outside the beryllium beam pipe to provide a precise measurement of the particle tracks. It consists of three main components which provide high-resolution detectors at inner radii and

sustained tracking elements at outer radii. This is very important for measuring the impact parameters and for vertex reconstruction. The ID is plunged in a magnetic field of 2 T provided by the central solenoid. All three systems are covering the pseudorapidity region of $|\eta| < 2.5$ and are further explained in the following.

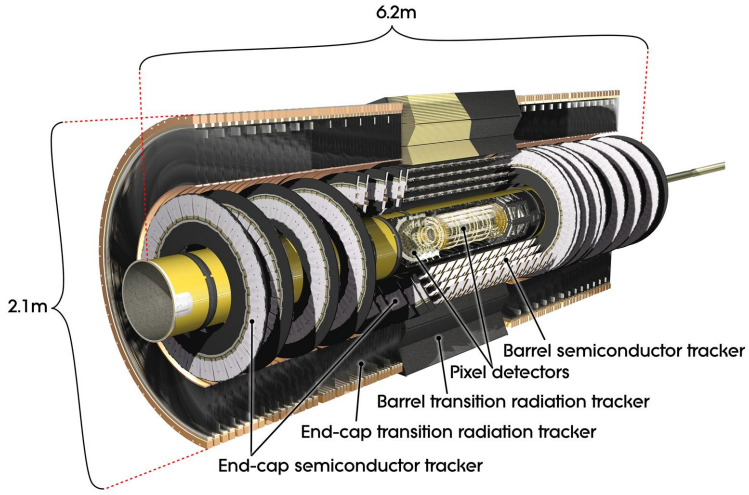

Figure 3.4: The ID of the ATLAS detector [21].

Pixel Detector

The pixel detector consists of three barrel layers and three disks of silicon pixel sensors. It can provide high-precision momentum and vertex measurements. In sum it is covering an area of 1.7 m^2. The pixel detector is crucial to reconstruct displaced vertices due to the decay of short lifetime particles like b hadrons or τ leptons due to its close position to the interaction point.

Semiconductor Tracker

The basic detector element of the Semiconductor tracker (SCT) uses silicon stripes instead of pixels. The SCT is composed of 4 cylindrical barrel layers and nine disks at each endcap. It covers an area of 61 m^2 and has readout-strips every 80 μm on the silicon. Its resolution is about 16 μm in the R-ϕ plane and about 580 μm in z direction [24].

Transition Radiation Tracker

The third component of the ID is the Transition radiation tracker (TRT). The TRT barrel consists of about 50000 gas-filled tubes called "straws", aligned parallel to the beam pipe, each 144 cm long and 4 mm in diameter. Every straw is equipped with a 30 μm gold-plated tungsten wire and filled with a mixture of Xe, CO_2 and CF_4. The endcap system consists of 250000 straws each 39 cm long and radially aligned [24].

3.2.4 The Electromagnetic Calorimeter

The electromagnetic calorimeter (ECAL) has an accordion-shaped geometry and surrounds the ID and the central solenoid. The detector elements consist of lead absorber plates and areas, filled with liquid argon (LAr) lying in-between. It is cooled down to its operating temperature point of 90.15 K. High energy particles propagating through the lead absorber plates are generating low energy particle-showers. These low energy particle-showers ionize the LAr between the absorber-plates. The ionized charge quantity in the LAr is measured by Kapton readout electrodes. The charge quantity is a measure of the energy of the passing high energy particle. The energy resolution of the calorimeter is $\Delta E/E = 10\%/\sqrt{E[\text{GeV}]} \oplus 0.7\%$ [25]. The ECAL consists of two identical half-barrels connected together with only a small gap of 6 mm in the z-x plane. On each endcap there are additional coaxial wheels. The barrel-part covers a pseudorapidity range of $|\eta| < 1.475$ and the wheels at the endcaps are covering the range of $1.375 < |\eta| < 3.2$.

3.2.5 The Hadronic Calorimeter

The Forward Calorimeter (FCAL) consists of three main parts: the scintillating Tile Calorimeter in the barrel region covering a pseudorapidity rage of $|\eta| < 1.7$, the Hadronic End-cap LAr Calorimeter (HEC) in the region of $|\eta| < 3.2$ and the FCAL. The Tile Calorimeter consists of plastic scintillator plates embedded in iron absorber. Over $1.5 < |\eta| < 4.9$ the calorimeter uses LAr as active material with copper and tungsten absorbers. To guarantee a good energy resolution of high energy jets and a precise measurement of the missing transverse energy E_T^{miss}, the important value is the thickness of the calorimeter. It must be thick enough to absorb almost all particles. For $\eta = 0$ the overall thickness is eleven interaction lengths (λs). This also avoids hadronic showers punching through into the outer muon spectrometer. The energy resolution of the tile calorimeter is $\Delta E/E = 50\%/\sqrt{E[\text{GeV}]} \oplus 0.3\%$ [26].

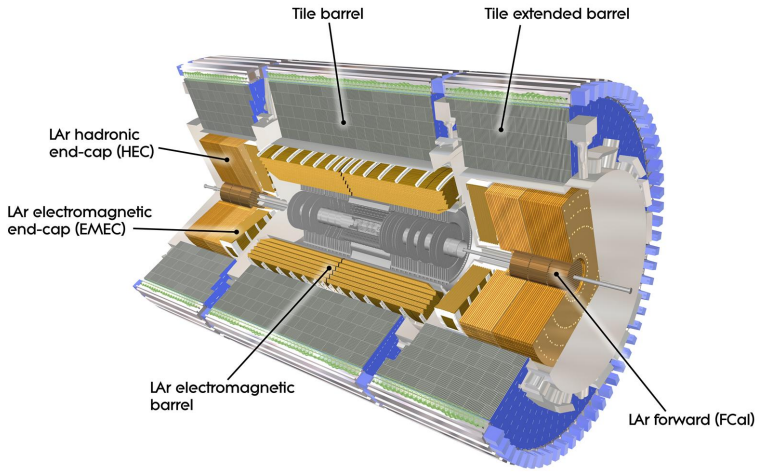

Figure 3.5: Hadronic and electromagnetic Calorimeter of ATLAS [21].

3.2.6 The Muon Spectrometer

Muons from a collision event imply important information for a proper reconstruction of the event. Because their interaction with matter is weak, they are not stopped in the inner detector parts. Consequently none of them will deliver sufficient information to distinguish between muons and other charged particles. For a precise measurement of their properties, the ATLAS detector has a muon spectrometer, which is the outermost part of the detector. Monitored Drift Tubes (MDTs) are installed over the range of $|\eta| < 2.7$, for a precise momentum measurement. The basic element of the MDTs is aluminum tube of 30 mm diameter with a 50 μm wire[1] in the centre. The wire is on an electrical potential of 3080 V. The tubes are filled with a mixture of Ar and CO_2 at three bar absolute pressure. Passing muons will ionize the contained gas. Then the ionized electrons multiply to charge avalanches due to the electric field. The charge quantity is measured. The single hit spatial resolution is about 80 μm [23].

At the range of $2 < |\eta| < 2.7$ are Cathode Strip Chambers (CSCs). These are multi-wire proportional chambers, providing a high readout rate which is needed in the forward region due to high charged particle rate. The precise measurement of the coordinates is achieved by quantifying the induced charge on the segmented cathode. Interpolation between adjoined strips and segmenting the readout cathode helps to improve the spatial resolution. The

[1]W-Re wire: Tungsten-Rhenium wire

resolution of the CSCs is about 60 μm [23].

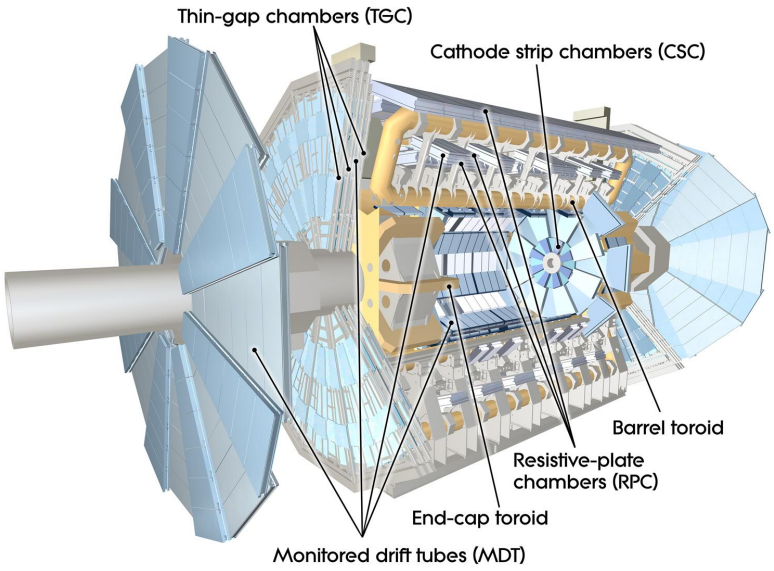

Figure 3.6: Complete muon spectrometer of ATLAS [27].

Two further systems, Resistive Plate Chambers (RPCs) and Thin Gap Chambers (TGCs) complete the muon spectrometer. They are mainly used for triggering on the muons. The basic element of the RPCs consists of two robust bakelite plates with a long and narrow gap, filled with gas[2]. A high electrical field of typically 4.5 kV multiplies ionized electrons to charge avalanches. The avalanches are measured by a capacitive coupling of metal strips on both sides. This system covers a pseudorapidity range of $|\eta| < 1.05$. In the range of $1.05 < |\eta| < 2.4$ TGCs, multi-wire proportional chambers[3] are used for triggering and a second spacial measurement.

3.2.7 Trigger and Data-Acquisition System

When the LHC operates at its design settings, the bunch crossing rate is 40MHz. Every bunch crossing can lead to several proton-proton interactions. Even at this high event rate, interesting events are rare compared to the overall event rate. Furthermore this large number of events cannot be stored. To reduce the number of events to a storable rate of about 500 Hz the ATLAS

[2]Mainly tetrafluoroethane ($C_2H_2F_4$).
[3]Filled with CO_2 and n-pentane (n-C_5H_{12}).

detector uses a multi-level selection system, the triggers. The trigger system consists of three stages: Level 1 (L1), Level 2 (L2), and Event Filter (EF).

The L1 trigger is a hardware based trigger. Its decision is based on high transverse momentum muons in the RPCs and TGCs trigger chambers, plus a reduced-granularity readout of the calorimeter. The calorimeter searches for high momentum electrons, photons, jets, τ-leptons and large missing transverse energies. The L1 trigger works at a frequency of about 100 kHz and passes selected events to the L2 trigger.

In the next step the selection of the L1 is processed by L2 triggers. These triggers are implemented in software. They utilize the region of interest (RoI) transmitted by the L1 triggers. With access to whole event information, it checks the event again for high momentum leptons, jets, missing and total transverse energy. The selection of the L2 runs at a frequency of about 3 kHz and passes the events to the EF.

The last stage of the trigger chain is the EF. The EF uses advanced algorithms to confirm the results of the L2 trigger decision. In the end it separates the events into data-streams depending on the fired triggers. For this analysis only the Muon and Egamma streams are used. The event rate after the EF is reduced to 300 Hz and the events are stored on data-tapes.

3.2.8 Computing

One single recorded event has a size of about 1.6 Mbytes. Consequently the ATLAS trigger data-acquisition system records about 320 Mbytes per second. In addition many Monte Carlo simulations are needed. This requires huge capacities in storage and computation. The EF information is written into RAW output files. The RAW data file size is about 1.6 Mbytes per event without pileup [28]. At CERN the reconstruction of the events is done. The output of the reconstruction process is called Event Summary Data (ESD). It is intended that the ESD format makes access to the RAW data unnecessary for the most physics applications. Its average file size is about 500 kBytes per event. The file size of the events is further reduced in the Analysis Object Data (AOD) files. The AOD file format is a reduced event representation, with an average size of 100 kBytes per event and has an object-oriented representation. A common used file format for end-user analysis is the Derived Physics Data (DPD). The data in the DPD has a n-tuple representation and it is a suitable format for direct analysis.

The ATLAS collaboration has many computing sites distributed around the world. The sites are classified in a tier structure. The CERN computing facility is the designated Tier0, where the primary processing happens. The recorded data is then distributed to eleven Tier1 sites [29]. Tier1 sites provide

further distribution and long term storage capacity. The third stage in the tier structure are Tier2 sites, typically computing centers at research labs or universities. They have enough data storage and computing power to do specific analysis tasks. Furthermore they are used to simulate the Monte Carlo events and they provide computing resources for user analysis. This collection of computing resources is collectively called the Worldwide LHC Computing grid. For this analysis, the first processing stage was achieved by using grid computing resources. The analysis itself used the resources of the Leibniz Supercomputing Centre (LRZ).

4 | Analysis Outline

The accurate measurement of W^+W^- production is an important cross-check of the SM prediction of the cross-section, consequently for the SM itself. In addition, a proper understanding of this process is essential for analyses where W^+W^- contributes to the background, for example in the decay channel of the Higgs Boson $H \to W^+W^-$. This analysis is an update of *"Measurement of the W^+W^- Production Cross Section in Proton-Proton Collisions at $\sqrt{s}$ = 7 TeV with the ATLAS Detector"* [30] using data recorded in the year 2012.

4.1 Signal Signature

The decay rate of a W boson into hadrons is about 67.6%. Therefore the probability for a W diboson pair decaying hadronically is 44.9%. However, the production cross-section for a QCD four jet event is much larger than the production cross-section of the W^+W^- boson pair. For that reason this analysis uses only the dileptonic decay channel of the boson pair. Since the decay fraction for $W \to l\nu \approx 10.8\%$ for $l = e$, μ, τ, the rate of the dileptonic channel is $\approx 10\%$. This analysis uses only events with e or μ in final state.

Figure 4.1 shows a tree level Feynman diagram of a W^+W^- boson pair decaying into two leptons and two neutrinos. The signal signature therefore is exactly two opposite charged leptons (electrons or muons). Since neutrinos can not be detected by the detector in a direct way, one looks for a relevant high missing transverse energy. Since one is expecting the dileptonic decay of the W^+W^- boson pair, events with jets are rejected.

The analysis is divided in three different channels according to the lepton flavor combination. The same flavor channels ee and $\mu\mu$ have different requirements in the event selection than the channel $e\mu$. Furthermore electrons and muons have different reconstruction and trigger efficiencies.

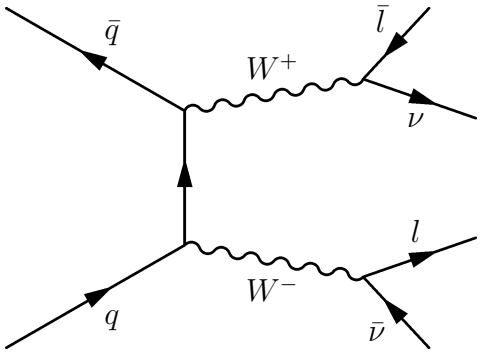

Figure 4.1: W^+W^- decay in leptonic channel.

4.2 Event Selection Criteria

The event selection is designed to separate the background processes discussed in section 2.3.2 from the signal processes. Therefore the following criteria need to be fulfilled:

- The event needs to have exactly two, oppositely charged, well reconstructed leptons. One leptons needs to have an transverse momentum of $p_T > 25\,\text{GeV}$. The other lepton needs to have a minimum p_T of 20 GeV. The lepton with the higher transverse momentum is called the leading lepton. In same flavor channels (ee, $\mu\mu$ channel) the invariant mass of the dilepton system $M_{l^+l^-}$ needs to be greater than 15 GeV. This selection suppresses Υ decays and multi-jet QCD events.

- In the $e\mu$ channel, the invariant mass is required to be greater than 10 GeV suppressing the low mass spectrum which is not covered in the Monte Carlo simulation.

- To suppress mainly the $Z \to l^+l^-$ decay, the invariant mass of the two leptons must not be within a 15 GeV region around the Z boson mass.

- The relative missing transverse energy $\not\!\!E_T^{rel}$ needs to be greater than 45 GeV in the same flavor channel, and greater than 25 GeV in the $e\mu$ channel. Hereby $\not\!\!E_T^{rel}$ is defined as:

$$\not\!\!E_T^{rel} = \begin{cases} \not\!\!E_T \times sin(\Delta\phi_{l,j}) & \text{if } \Delta\phi_{l,j} < \pi/2 \\ \not\!\!E_T & \text{if } \Delta\phi_{l,j} \geq \pi/2 \end{cases}$$

  with $\Delta\phi_{l,j}$ being the difference in ϕ of $\not\!\!E_T$ and the closest lepton or jets. The usage of the perpendicular projected $\not\!\!E_T$ helps to reduce the sensitivity to misidentified leptons or jet, leading to a mismeasured $\not\!\!E_T$.

- Events containing jets with transverse energy $E_T > 25\,\text{GeV}$ and a pseudorapidity of $|\eta| < 4.5$ are rejected, since the dileptonic decay channel of W^+W^- includes no jets.

- The di-lepton transverse momentum needs to be greater than 45 GeV in the same flavor channel and over 25 GeV in the $e\mu$ channel.

4.3 Changes to the $\sqrt{s} = 7\,\text{TeV}$ Analysis

Since the center of mass energy has been raised from $\sqrt{s}$ =7 TeV to $\sqrt{s}$ =8 TeV, the analysis was changed for further optimization and to deal with the higher pileup of the events. The changes are:

- The lepton object definition was changed, to be consistent with other analysis groups. This helps to compare fake rates and background estimates between different analyses. The vertex requirements are tighter in comparison to the old analysis. Also, the requirements for the calorimeter and track isolation are stricter.

- A new algorithm[1] for the jet reconstruction is used. Furthermore, the cut on the jet vertex fraction of $|JVF| > 0.5$ is only applied to jets with $E_T < 50\,\text{GeV}$ and $|\eta| < 2.4$.

- The selection for the di-lepton momentum is now different for the same flavor channel and the $e\mu$ channel. Studies about cutflow optimization showed that the old cut value could be optimized.

4.4 Cross-section calculation

The total cross-section is calculated by

$$\sigma_{W^+W^-} = \frac{N_{obs} - N_{bkg}}{\mathcal{L} \cdot \mathcal{A}\epsilon \cdot \text{BR}} \tag{4.1}$$

where N_{obs} is the number of observed events in the signal region. The number of expected background events N_{bkg} is estimated by counting the Monte Carlo simulated events or data-driven background estimate in the same region. The total usable integrated luminosity $\mathcal{L}$ is $20.1\,\text{fb}^{-1}$. The acceptance $\mathcal{A}$ and the efficiency ϵ is treated as one number, the total efficiency

[1] "AntiKt4 LC" instead of "AntiKt4 EM".

$\mathcal{A}\epsilon$. The branching ratio BR is given by the dileptonic branching fraction of a W diboson event. This equation can be simplified to

$$\sigma_{W^+W^-} = \sigma_{NLO} \cdot \frac{N - B}{S}, \tag{4.2}$$

where $S = \sigma_{NLO} \cdot \mathcal{L} \cdot \mathcal{A}\epsilon \cdot \mathrm{BR}$. In this formula N stands for the number of observed events and B for the number of background events, $\mathcal{L}$ the integrated luminosity of $20.1\,\mathrm{fb}^{-1}$, and BR the dileptonic branching ratio of the W^+W^- pair $\mathrm{BR} = 0.1080 \pm 0.0009$ [9].

4.4.1 Uncertainties on the Measurement

The statistical uncertainties for the cross section can be calculated with the Gaussian approximation. The uncertainty is given by

$$\frac{\Delta_{\mathrm{stat}}\sigma_{W^+W^-}}{\sigma_{W^+W^-}} = \frac{\sqrt{N}}{N - B}. \tag{4.3}$$

The uncertainties derived with data driven methods are expected to not to be correlated with the uncertainties on the signal efficiency. They can be calculated using the Gaussian error propagation:

$$\frac{\Delta_{\mathrm{syst}}\sigma_{W^+W^-}}{\sigma_{W^+W^-}} = \sqrt{\left(\frac{\Delta A\epsilon}{A\epsilon}\right)^2 + \left(\frac{\Delta B}{N - B}\right)^2 + \left(\frac{\Delta \mathrm{BR}}{\mathrm{BR}}\right)^2}. \tag{4.4}$$

The uncertainty for the luminosity is 2.8%. It can be taken into account with the following formula:

$$\frac{\Delta_{\mathrm{lumi}}\sigma_{W^+W^-}}{\sigma_{W^+W^-}} = \sqrt{\left(\frac{\Delta\mathcal{L}}{\mathcal{L}}\right)^2 + \left(\frac{B_i}{N - B}\frac{\Delta\mathcal{L}}{\mathcal{L}}\right)^2}, \tag{4.5}$$

where B_i stands for each of the background simulation used.

4.4.2 Overview of W^+W^- Production Cross Section Measurements

The W^+W^- production cross section was first measured at the LEP2. Since then the production cross section of the diboson was measured in several experiments. This section lists measurements of the production cross section at different experiments.

LEP2

The LEP2 was an electron-positron collider operating at center of mass energies above the Z-pole [31]. The measured W^+W^- cross section for the center of mass energy of $\sqrt{s} = 206.6\,\text{GeV}$ is

$$\sigma_{\text{LEP2}} = 17.15 \pm 0.25\,\text{pb}.$$

TeVatron

TeVatron is an proton-antiproton collider with a center of mass energy of $\sqrt{s} = 1.96\,\text{TeV}$. The W^+W^- cross section measured was measured with the experiments D0 [32] using data collected $1\,\text{fb}^{-1}$. The result is

$$\sigma_{\text{D0}} = 11.5 \pm 2.1\,(\text{stat} + \text{syst}) \pm 0.7\,(\text{lumi})\,\text{pb}.$$

CDF was using $3.6\,\text{fb}^{-1}$ collected data from proton-antiproton collisions at the same center of mass energy [33]. The measured W^+W^- cross section is

$$\sigma_{\text{CDF}} = 12.1 \pm 0.9\,(\text{stat})\,^{+1.6}_{-1.4}\,(\text{syst})\text{pb}.$$

The W^+W^- cross section prediction of the SM under this conditions is $\sigma_{\text{NLO}} = 11.7 \pm 0.7\,\text{pb}$. Both measurements are in agreement with the prediction.

LHC

At the LHC the cross section for the W^+W^- production process was measured with $\sqrt{s} = 7\,\text{TeV}$ and $\sqrt{s} = 8\,\text{TeV}$. The measurement of the W^+W^- cross section uses $4.7\,\text{fb}^{-1}$ of collected data in proton proton collisions at a center of mass energy of $\sqrt{s} = 7\,\text{TeV}$ [30][34]. The result of the ATLAS collaboration is

$$\sigma_{\text{ATLAS,7 TeV}} = 53.4 \pm 2.1\,(\text{stat}) \pm 4.5\,(\text{syst}) \pm 2.1\,(\text{lumi})\,\text{pb}.$$

The measured W^+W^- cross section from the CMS experiment with data corresponding to an integrated luminosity of $4.92\,\text{fb}^{-1}$[35] is

$$\sigma_{\text{CMS,7 TeV}} = 52.4 \pm 2.0\,(\text{stat}) \pm 4.5\,(\text{syst}) \pm 1.2\,(\text{lumi})\,\text{pb}.$$

All these measurements are in agreement with the $\sigma_{\text{NLO}} = 47.0^{+2.0}_{-1.5}$.

The center of mass energy for the 2012 data taking period was at $\sqrt{s} = 8\,\text{TeV}$. Using data corresponding to $5.3\,\text{fb}^{-1}$ [36] of integrated luminosity, CMS obtained an W^+W^- production cross section of

$$\sigma_{\text{CMS,8 TeV}} = 69.9 \pm 2.8\,(\text{stat}) \pm 5.6\,(\text{syst}) \pm 3.1\,(\text{lumi})\,\text{pb}.$$

This result is slightly higher than the predicted cross section of $\sigma_{NLO} = 57.22\,\text{pb}$.

5 | Particle Identification

Most particles appear in the detector as tracks in the detector subsystems or deposits in calorimeters. A proper reconstruction of the physics objects is crucial to understand the collision event. The following section explains what requirements are used to classify the physics objects.

5.1 Electrons

Electrons interact with the ID and the electromagnetic calorimeter. They leave tracks in the ID and energy deposits in the calorimeter. In order to reconstruct an electron a track is matched to the deposits in the calorimeter. There are two recommended ways to identify an electron. Either it is reconstructed by a cluster-based algorithm, or an algorithm, which combines a cluster and track-based method [37].

In this analysis, electrons must be reconstructed by one of the algorithms. Furthermore geometrical and kinematic requirements are applied. Detector regions with read-out problems are excluded. The exact values of applied selection criteria are listed in table 5.1. An electron can be classified by three basic types: loose++, medium++, and tight++. These are defined sets of selection criteria based on the shower shape, track quality and the matching of the track to the calorimeter deposits [38]. This analysis uses tight++ classified electrons, since the probability for misidentified electrons is lower than it is for the other criteria. The electron needs to be a single isolated electron, and should have its origin in a collision event. Therefore it is required that the sum of transverse energy within a cone of $\Delta R = 0.3$ must be less than 16% of the electron transverse energy. The track must be isolated as well: the sum of transverse momentum must be less than 12%, and 16% for electrons with $p_T > 25\,\text{GeV}$, of the electron transverse momentum.

Electron selection criterion	
Reconstruction:	cluster-based or combined cluster and track-based algorithm
Pseudorapidity:	$\|\eta\| < 2.47$, exclude crack region $1.37 < \|\eta\| < 1.52$
Quality:	exclude regions with calorimeter red-out problems
Transverse Energy:	$E_T > 20\,\text{GeV}$
Identification:	Tight++
z_0:	$\|z_0 \cdot \sin(\theta)\| < 0.4\,mm$
d_0 significance:	$d_0/\sigma(d_0) < 3$
Calorimeter Isolation:	$((\Sigma_{\Delta R<0.3} E_{T,i} - E_{T,el})/E_{T,el}) < 0.16$
Track Isolation:	$((\Sigma_{\Delta R<0.3} p_{T,i} - p_{T,el})/p_{T,el}) < 0.12$ or 0.16 for electrons with $E_T > 25\,\text{GeV}$

Table 5.1: This table shows the electron selection criteria. z_0 is the longitudinal and d_0 the transverse impact parameter

5.2 Muons

There are two basic muon reconstruction algorithms, "MuID" and "STACO" [39]. The selected muons in this analysis must be reconstructed by the "STACO" algorithm. This algorithm has basically three ways to reconstruct a muon: "standalone", "combined", and "tagged". The "standalone" criteria uses only information measured by the muon spectrometer as explained in section 3.2.6. The tracks of the muon are extrapolated to the interaction vertex. The energy loss of the muon in the calorimeter is taken into account. A "combined" classified muon uses the tracks of the muon spectrometer. These tracks are fitted and extrapolated back to the interaction vertex. Furthermore these tracks are matched with tracks observed in the ID and combined to one single track. The reconstruction variant of muons "tagged" is using the tracks from the ID. These tracks are extrapolated to the muon spectrometer. In case one extrapolated Track from the ID matches one measured track in the muon spectrometer, it is denoted as a reconstructed muon.

The muon selection is similar to the electron selection. The reconstruction method used for the muons in this analysis is "combined". First of all, geometrical and kinematic requirements must be fulfilled. A set of hit requirements in each subdetector need to be satisfied. Moreover the energy

deposits in the calorimeter and the tracks must be isolated. The exact values for the selection are listed in table 5.2.

Muon selection criterion	
Reconstruction:	combined
Pseudorapidity:	$\|\eta\| < 2.4$
Transverse Energy:	$p_T > 20\,\text{GeV}$
ID Quality:	minimum recommended detector hits
z_0:	$\|z_0 \cdot \sin(\theta)\| < 1\,mm$
d_0 significance:	$d_0/\sigma(d_0) < 3$
Calorimeter Isolation:	$(\Sigma_{\Delta R<0.3} E_{T,i}/p_{T,\mu}) < 1.4 \cdot 10^{-5} \cdot p_{T,\mu} - 0.15$ and $(\Sigma_{\Delta R<0.3} E_{T,i}/p_{T,\mu}) < 0.015$
Track Isolation:	$(\Sigma_{\Delta R<0.3} p_{T,i}/p_{T,\mu}) < 10^{-5} \cdot p_{T,\mu} - 0.105$ and $(\Sigma_{\Delta R<0.3} p_{T,i}/p_{T,\mu}) < 0.015$

Table 5.2: The muon selection criteria. z_0 is the longitudinal and d_0 the transverse impact parameter

5.3 Jets

Since quarks are color charged, they can not be observed in isolation. They combine to bound states, via hadronization and color reconfinement. These objects can be observed as jets.

The reconstruction of the jet is based on the anti-k_T [40] jet clustering algorithm. The algorithm calculates every distance between calorimeter entries according to a certain distance measure [41]. In case the entry is closer than a predefined distance ΔR, they are clustered together and will be treated as one object. This procedure is repeated till every object in the given distance ΔR is clustered together. This object is then a reconstructed jet.

In this analysis the defined resolution parameter for the anti-k_T algorithm is $\Delta R = 0.4$. The jets are calibrated by the "LC+JES" method [42]. Selected jets must fulfill a minimum transverse momentum of $p_T > 25\,\text{GeV}$ and lie within the pseudorapidity region of $|\eta| < 4.5$. The jet vertex fraction measures the probability that a jet originated from a particular vertex [43]. Jets in the barrel region of $|\eta| < 2.4$ and up to a transverse momentum of

$p_T = 50\,\text{GeV}$ are required to have a jet vertex fraction of over 0.5 in order to suppress pileup effects.

5.4 Lepton-Lepton and Lepton-Jet Overlap

As explained in section 5.3, jets are reconstructed by a clustering algorithm, which iterates over energy deposits in the calorimeter. Consequently electrons are reconstructed as jets. Furthermore muons can leave bremsstrahlung which can be misidentified as a collision electron. In order to suppress these misidentification effects, leptons must not overlap with other reconstructed leptons or jets. Selected electrons within a cone of $\Delta R = 0.1$ to selected muons or other electrons, are rejected. Jets within a cone of $\Delta R = 0.3$ to selected electrons or muons, are rejected as well.

5.5 Missing Transverse Energy

Some particles, like neutrinos can not be detected directly by the ATLAS detector, however they carry away momentum. One can estimate the missing energy by summing over all collected energies from the electromagnetic and hadronic calorimeter, and the measured muon momenta. The $\not\!\!E_T$ is defined by

$$\not\!\!E_T := \sqrt{(\Sigma E_x)^2 + (\Sigma E_y)^2}.$$

For this analysis the $\not\!\!E_T$ is an important value to distinguish a W boson pair from background processes, since the W boson decays into a lepton-neutrino pair. Compared to a Z boson decay into two leptons, the W decay causes missing energy, but the $\not\!\!E_T$ in Z decay is close to zero.

Misidentified leptons or jets lead to a mismeasured $\not\!\!E_T$. In order to reduce the sensitivity of the $\not\!\!E_T$ caused by to miss-measurement the perpendicular projected $\not\!\!E_T$ is introduced. The relative missing transverse energy $\not\!\!E_T^{rel}$ is defined by

$$\not\!\!E_T^{rel} = \begin{cases} \not\!\!E_T \times sin(\Delta\phi_{l,j}) & \text{if } \Delta\phi_{l,j} < \pi/2 \\ \not\!\!E_T & \text{if } \Delta\phi_{l,j} \geq \pi/2 \end{cases} \tag{5.1}$$

where $\Delta\phi_{l,j}$ is the difference in ϕ of $\not\!\!E_T$ and the closest lepton or jet.

5.6 Track-based Missing Transverse Momentum

The missing p_T^{miss} is calculated as the vectorial sum over all tracks from the primary vertex. For these calculation the tracks must fulfill different requirements which are listed in table 5.3. Tracks of signal muons are included regardless to the measured quality and tracks of signal electrons are replaced by the transverse energy, measured by the calorimeter.

The p_T^{miss} is less sensitive to mismeasurements due to the higher pileup rate. It helps to distinguish a W^+W^- signal from the main background in the same flavor channel, the Z+jets background which is explained in section 10.2.

Track requirements	
Transverse momentum:	$p_T > 500\,\text{MeV}$
Pseudorapidity:	$\lvert\eta\rvert < 2.5$
z_0:	$\lvert z_0 \cdot \sin(\theta)\rvert < 1.5\,mm$
d_0:	$d_0 < 1.5\,mm$
Pixeldetector hits:	$n_{Pixel} \geq 1$
SCT hits:	$n_{SCT} \geq 6$

Table 5.3: Track requirements used for the calculation of the missing transverse momentum.

6 | Signal and Background Monte Carlo Samples

6.1 Monte Carlo Simulations

For a proper understanding of the recorded data, it is necessary to simulate proton-proton collisions. The simulation consist of three stages [44]. At first, the hard process is simulated. This is done using the event generator, which simulates the collisions of partons as they would happen in the detector. In a second stage the generated particles undergo the parton showering. This means, the hadronization of color-charged particles is simulated, as well as further decays of the hadrons. After an event is simulated completely, one needs to simulate the response, which the ATLAS detector would give measuring such an event. For this the Geant4 framework is used [45].

6.1.1 Event Generators

There are several Monte Carlo (MC) event generators available. They distinguish in the process they are modeling and in higher order calculation. Consequently, for different process simulations, different generators are used. The following section gives an overview, which generator was used for the different signal and background processes.

W^+W^- Processes

W diboson production from quark initial states, decaying fully leptonic $q\bar{q} \rightarrow W^+W^- \rightarrow l^+\nu_l l^-\bar{\nu}_l$, is generated by POWHEG. It includes several standard model processes like the diboson or single top production [46][47]. It is capable to calculate next-to-leading order matrix elements. For parton showering algorithms POWHEG uses another generator named PYTHIA [48]. The W^+W^- production via gluon initial states is modeled by a generator called gg2WW [49]. This generator is specialized for exactly this process, and uses

HERWIG for modeling the parton showering and multiple parton scattering. Furthermore the SM Higgs decay to W^+W^- is added. In this process the SM, with a mass of $m_H = 125\,\text{GeV}$ is generated by gluon gluon fusion. The event generator used is POWHEG with the parton showering methods from PYTHIA.

Background Processes

The major background processes are listed in section 2.3.2. These are mainly events of a single W or Z boson with associated jets and top events. Processes with a gauge boson and associated jets are simulated with ALPGEN. This generator is specialized for processes with a fixed number of partons and high jet multiplicity in the final states [50]. MC@NLO is a next-to-leading order generator, which calculates QCD processes [51]. Therefore it is used to model the $t\bar{t}$ and single top events. Since it is not able to simulate the hadronization for the jets, it is interfaced to AcerMC. As mentioned in section 6.1.1 POWHEG is a generator which is able to model proper diboson events, like ZZ and WZ. For this reason it is used to model this diboson background. The process of $W\gamma*$ can as well have the same signature as the dileptonic decay of W^+W^-. In this case the massive virtual photon decays dileptonically [52]. This process with a massive photon is modeled by MadGraph, interfaced to Pythia as showering MC generator.

6.2 Corrections to Monte Carlo Events

Simulated events are already very well modeled to real measured data. However some effects are not included in the modeling of the MC generators. These effects, like lepton efficiency measurements or a higher average interactions per proton bunch crossing rates, need to be corrected using external software packages. All correction factors are obtained from software provided by the ALTAS Collaboration.

6.2.1 Pileup and Vertex Reweighting

The MC samples are usually produced before the data taking period starts. Therefore it is not possible to know the exact pileup conditions of recorded data [53]. In order to correct the default pileup in the simulations, the events needs to be reweighted to fit the real pileup conditions. Similarly to the pileup reweighting, there is as well a reweighting to the position of the hard interaction vertex applied.

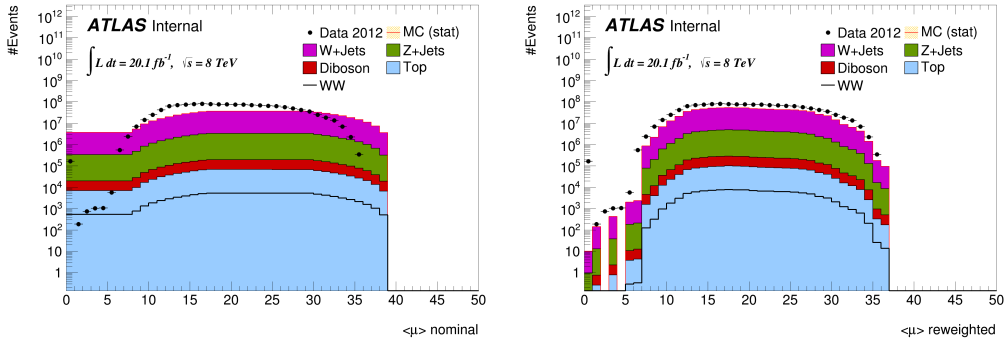

(a) Nominal (b) Reweighted

Figure 6.1: The average interaction per bunch crossing $<\mu>$, 6.1a the nominal distribution and 6.1b after pileup weights are applied. Single top and $t\bar{t}$ processes are summarized under "Top". ZZ, WZ, $W\gamma$, and $W\gamma*$ processes are combined into "Diboson".

6.2.2 Electrons

The electron efficiency of the ID is determined using a tag-and-probe method in $Z \to e^+e^-$ events [54]. The efficiency scale factors are applied to match the efficiency in the data. In addition with the use of calibration measurements in $W \to e\nu$ and $Z \to e^+e^-$, the electron energy scale is corrected in data and smeared in MC simulation. The calorimeter energy isolation cone of the electrons is corrected to settle transverse leakage of the electron shower in the cone [55].

6.2.3 Muons

The efficiency of the muons has been measured using $Z \to \mu\mu$ events. As for the electrons, the muons are reweighted [56], such that the simulated muon efficiency matches to the measured muon efficiency in data. Furthermore, the momentum of the muons is scaled in such a way that the direction of the muons remains unchanged.

6.2.4 Jets

The pileup correction has a larger effect to the data recorded in the 2012 run [42]. Therefore the old method of correcting the energy scale of the jets was improved. The new correction technique implies several stages of correction

[57]. The clusters are calibrated based on their properties. Afterwards the Jet is corrected depending on the pileup. The jet direction is changed to point to the primary vertex. Hereafter the absolute EtaJES correction is applied. This calibrates the four-momentum and the direction of the jet. Finally a correction based on the tracking is applied, which reduces flavor dependence.

6.2.5 Lepton Trigger Scale Factors

Lepton trigger efficiencies are measured with a tag-and-probe method in $Z \rightarrow l^+l^-(l \in [e, \mu])$ events. This is done in data and MC events. In order to bring the efficiency of the triggers in agreement with the measured efficiency, scale factors are calculated in the following way:

$$SF = \frac{1 - \Pi_i(1 - \epsilon_i^{Data})}{1 - \Pi_i(1 - \epsilon_i^{MC})}. \tag{6.1}$$

In this formula ϵ_i stands for the measured efficiency in data and MC respectively. The scale factors are applied to the MC events.

7 | Data Sets

7.1 Recorded Data from the ATLAS Detector

The data taking period for pp collisions in the year 2012 started an 26th March and ended on the 17th December. Figure 7.1 shows the integrated luminosity for the year 2012. The green line depicts the luminosity delivered by the LHC. Integrated over the whole period, it sums up to $\mathcal{L}_{LHC} = 23.3\,\text{fb}^{-}1$. The yellow line shows the luminosity recorded by the ATLAS detector, during stable beam conditions. The integrated luminosity recorded is $\mathcal{L}_{ATLAS} = 21.7\,\text{fb}^{-}1$. The Luminosity is determined by luminosity detectors, which are calibrated using the van-der-Meer beam-separation method [18]. The beams are vertically and horizontally crossed, in order to determine their overlap function.

The recorded data underwent a general reprocessing in the summer of 2012. The reprocessing was motivated by improving the data quality to resolve several issues, as for example the alignment in the ID and the muon spectrometer were modified [58].

7.2 Event Cleaning

There are some events, which do not fulfill the quality standard for recorded data. These problematic events need to be removed. This sections lists the quality standards defined by the Standard Model group.

7.2.1 Data Quality

High data quality is only guaranteed when all components of the ATLAS detector are running properly. Therefore events must be in the "Good Run List". This is an auto-generated list of luminosity blocks considered to have good data quality.

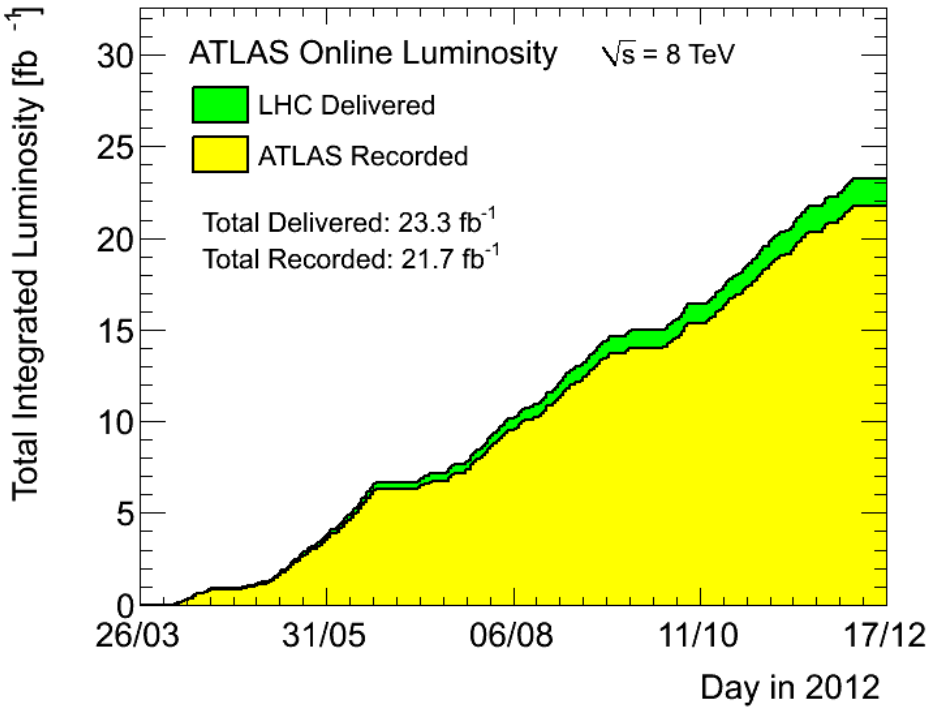

Figure 7.1: This plot shows the integrated luminosity $\mathcal{L}$ on a day-scale during the 2012 run. The green line illustrates the delivered integrated luminosity by the LHC, the yellow line shows the recorded luminosity by the ATLAS detector [18].

7.2.2 Detector Flags

The liquid argon calorimeter has occasional noise bursts [59]. These bursts are distorting the exact measurement of the energy. The recorded events are automatically detected and flagged. Problematic[1] events are rejected.

7.2.3 Hot Tile Calorimeter

In rare cases during the data taking period B1 and B2 there was a problematic module in the tile calorimeter. It is recommended that events with jets, pointing close to a certain region in η and ϕ, are rejected [60].

[1]Detector flags: "lArError", "TileError".

7.2.4 Stream Overlap

As mentioned in section 7.1, this analysis uses the "Egamma" and "Muon" stream. This means data is written out to streams depending on the fired triggers. In cases, in which electron or γ triggers and muon triggers are fired, the event is exported to both streams. In order to avoid a double counting of events, this overlap can be dropped out in a simple way. First, the whole "Muon" stream is processed. The events of the "Egamma" stream are then tagged if they are exported to both streams. Since these events would appear twice in the analysis, they are rejected.

7.2.5 Missing Transverse Energy Cleaning

Some energy deposits in the calorimeter can be reconstructed as "bad jets". If these bad jets are not matchable to reconstructed muons or electrons, it indicates that they have their origin in hardware problems or cosmic ray showers. Since these misidentified jets would distort the calculation of the missing transverse energy, the whole event has to be rejected. Therefore jets, tagged as "bad jets"[2], and greater transverse momentum than 20 GeV, not overlapping with a lepton with a cone of $\Delta R = 0.3$ are rejected.

7.2.6 Lepton Trigger

This analysis uses a combination of single lepton triggers. These four triggers are listed in table 7.1. For example "EF_mu36_tight" stands for an event-filter level muon trigger with a p_T threshold of 36 GeV. The tight means the object has to fulfill a tight selection of quality criteria. There are further muon and electron triggers available. In case one of them is fired the event is exported to the "Egamma" or "Muon" stream. This analysis requires one of the four lowest unprescaled single-lepton triggers, which are listed in table 7.1. Therefore the data streams are filtered correspondingly to at least one of these triggers is fired.

[2]Defined set of criteria according to the official recommendation.

Lepton	Trigger
Muon	EF_mu24i_tight
	EF_mu36_tight
Electron	EF_e24vhi_medium1
	EF_e60_medium1

Table 7.1: Event-filter level single lepton triggers. In analyzed events it is required that at least one of these triggers has fired.

8 | Event Selection

The dileptonic decay $W^+W^- \to l^+\nu_l l^-\bar{\nu}_l$ can be categorized into three topologies: $e^+e^- + \not{E}_T$, $\mu^+\mu^- + \not{E}_T$ or $e^\pm\mu^\mp + \not{E}_T$. All these three channels have the same event preselection. The preselection includes the requirements for general data quality criteria and is described in section 8.1. The event selection, described in section 4.2, is channel dependent. The $\not{E}_T^{rel}$, the Z veto, and the $p_{T,ll}$ cuts are different for the same flavor channels compared to the $e\mu$ channel.

8.1 Event Preselection Criteria

The preselection criteria for MC are explained in section 6.2, and the data event cleaning is explained in 7.2. In the following the applied preselection criteria are summarized.

- **Data Quality:** Events are filtered with respect to the data quality criterion by the GoodRunList as described in section 7.2.1.
- **Detector Flags:** Events affected by LAr noise bursts or tagged as problematic as described in section 7.2.2, are removed.
- **Hot Tile Calorimeter:** Events with Jets pointing in the problematic region of the tile calorimeter during the run B1 and B2 are removed. This is described in section 7.2.3.
- **Primary Vertex Tracks:** The reconstructed primary vertex needs to have at least three associated tracks. Otherwise the events are dropped.
- **Stream Overlap Removal:** Events appearing in the "Egamma" and "Muon" stream, since a muon and an electron or γ trigger has fired. This is described in section 7.2.4 and duplicated events are removed from the "Egamma" stream.

- **Trigger Selection:** As explained in section 7.2.6 this analysis requires at least one of the lowest unprescaled single lepton triggers. The triggers are "EF_e24vhi_medium" or "EF_e60_medium" for electrons, and for muons "EF_mu24i_tight" or "EF_mu36_tight". If none of these trigger has fired the event is rejected.

- **Dilepton Selection:** This analysis uses only the dileptonic decay channel of the W^+W^-, which should yield two leptons in the final state. Every event containing more than two leptons are dropped.

- $\not{E}_T$ **Cleaning:** Misinterpreted energy deposits in the calorimeter can lead to a distorted $\not{E}_T$ calculation. Therefore events where "bad jets" are not overlapping with leptons, are removed. This is described in section 7.2.5.

- **Oppositely Charged Leptons:** Since the charge is conserved, one expects two oppositely charged leptons from W^+W^- decay. If the leptons have the same charge, they can not result from a W^+W^- decay. These events are rejected.

- **Leading Lepton** p_T**:** The leading lepton should have a momentum $p_T > 25\,\text{GeV}$. This is important to reach the plateau of the trigger efficiency and enables the use of the trigger scale factors.

- **Trigger Matching:** First one of the lowest unprescaled lepton triggers was required to fire. Furthermore the fired trigger must be assigned to one of the both leptons. This is called trigger matching. Events where triggers and leptons can not be matched together are rejected.

8.1.1 Kinematic Distributions after Preselection

This section shows kinematic distributions and the cutflow table of selected variables after they passed the preselection criteria. In the following plots and tables, similar background processes (see section 2.3.2) are combined together. Single top and $t\bar{t}$ processes are summarized under "Top". ZZ, WZ, $W\gamma$, and $W\gamma*$ processes are combined into "Diboson". The label "Z+Jets" denotes processes where $Z/\gamma*$ decays and can have associated jets. The cutflow table of the preselection is given in Table 8.1. Figure 8.1 shows the invariant mass of the reconstructed leptons. The $\not{E}_T^{rel}$ is depicted in figure 8.2 and dileptonic momenta of the leptons is shown in figure 8.3. Figure 8.4 shows the jet multiplicity.

Criterion	W^+W^- prediction	Total MC	Data
Initial	122.678 ± 70	$856.920.000 \pm 210.000$	1.449.498.968
Data Quality	122.678 ± 70	$803.260.000 \pm 200.000$	1.357.047.402
Detector Flags	122.678 ± 70	$803.260.000 \pm 200.000$	1.354.272.708
Tile Calorimeter	122.678 ± 70	$803.260.000 \pm 200.000$	1.354.272.708
FCAL Cleaning	122.678 ± 70	$803.260.000 \pm 200.000$	1.354.272.708
Primary Vertex	122.235 ± 70	$797.860.000 \pm 200.000$	1.350.402.614
Pileup Weight	122.255 ± 80	$798.130.000 \pm 230.000$	1.350.402.614
Vertex Weight	121.675 ± 84	$847.600.000 \pm 250.000$	1.350.402.614
Stream Overlap	121.675 ± 84	$847.600.000 \pm 250.000$	1.338.044.076
Trigger	72.176 ± 65	$247.210.000 \pm 130.000$	525.903.722

Table 8.1: Cutflow table after applied criteria of the preselection. The simulated events are scaled to an integrated luminosity of $20.1\,\mathrm{fb}^{-1}$. Since a simulation for the QCD background is not used, there is a discrapency between data and MC.

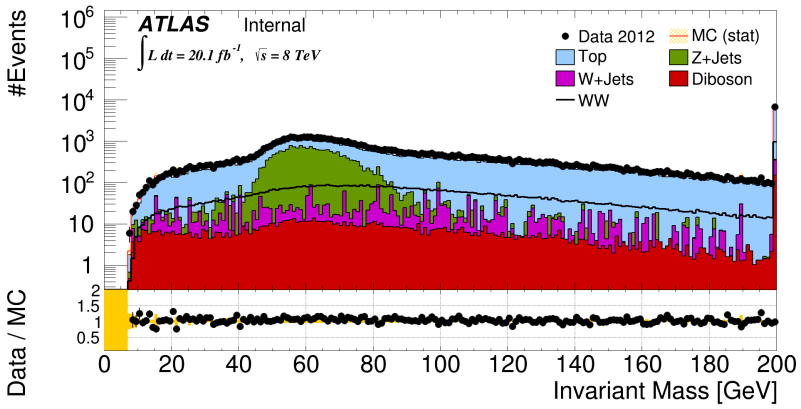

(a) $e\mu$ channel

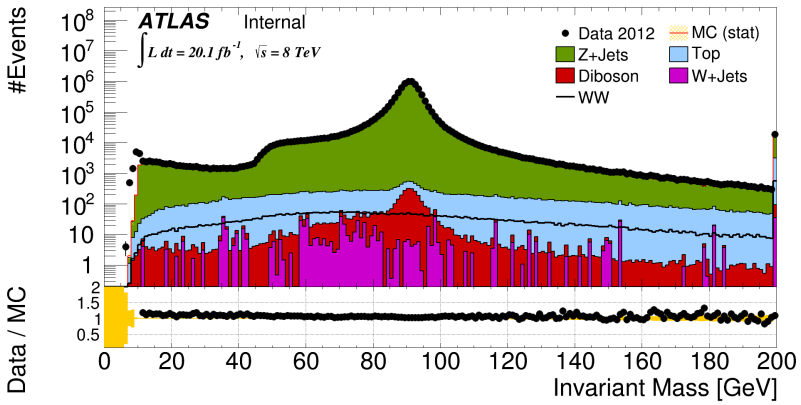

(b) $\mu\mu$ channel

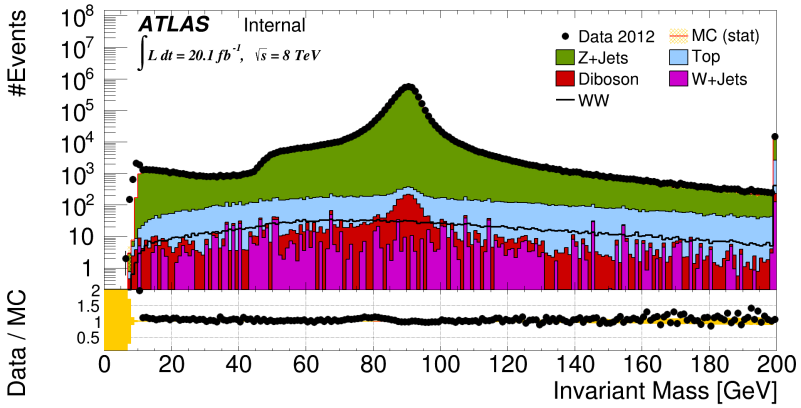

(c) ee channel

Figure 8.1: The invariant mass $M_{l^+l^-}$ of the dilepton system after all preselection criteria are applied. On top for $e\mu$ channel, middle $\mu\mu$ channel, and at bottom ee. The last bin is the overflow bin. It contains all events with a invariant mass greater than 200 GeV.

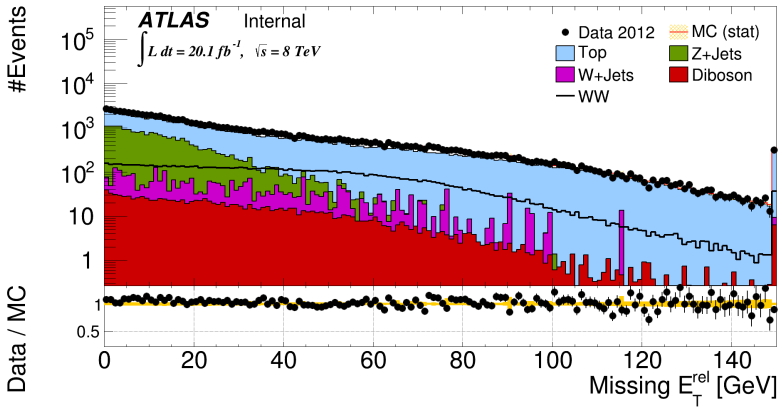

(a) $e\mu$ channel

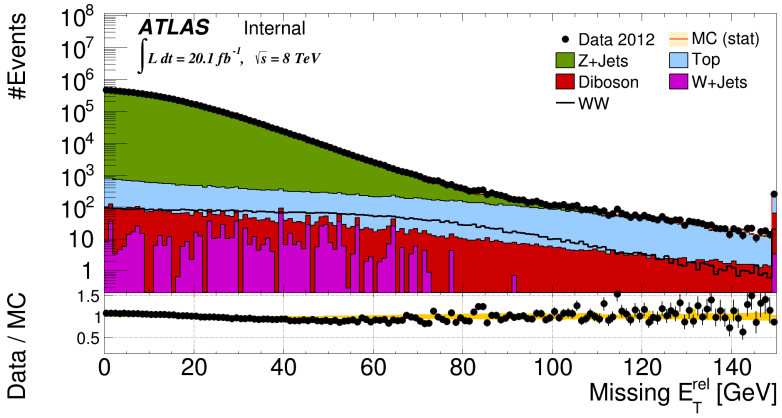

(b) $\mu\mu$ channel

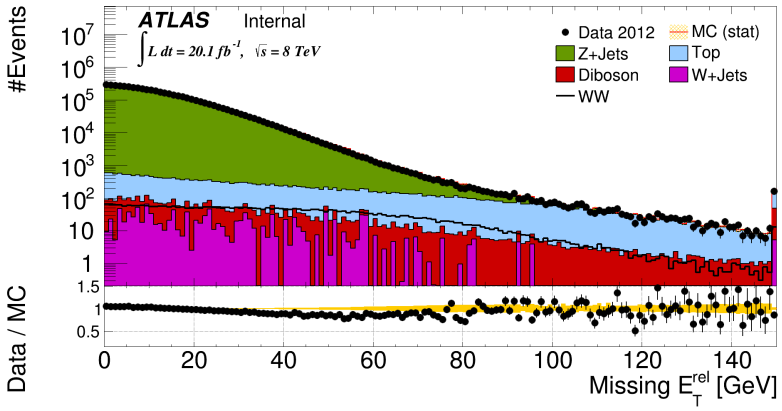

(c) ee channel

Figure 8.2: The $\not{E}_T^{rel}$ distribution. On top for $e\mu$ channel, middle $\mu\mu$ channel, and at bottom ee.

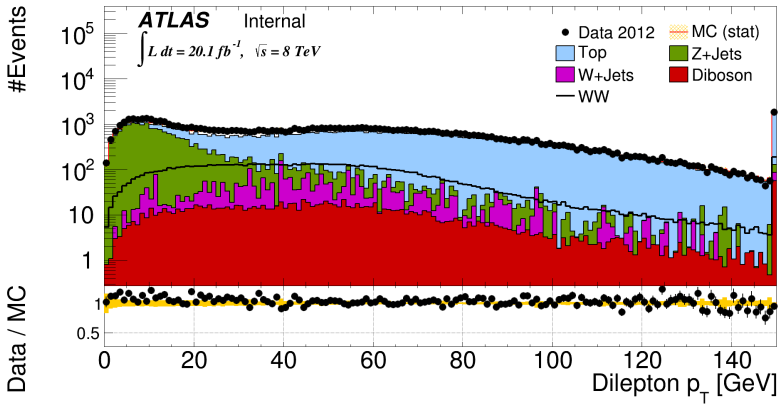

(a) $e\mu$ channel

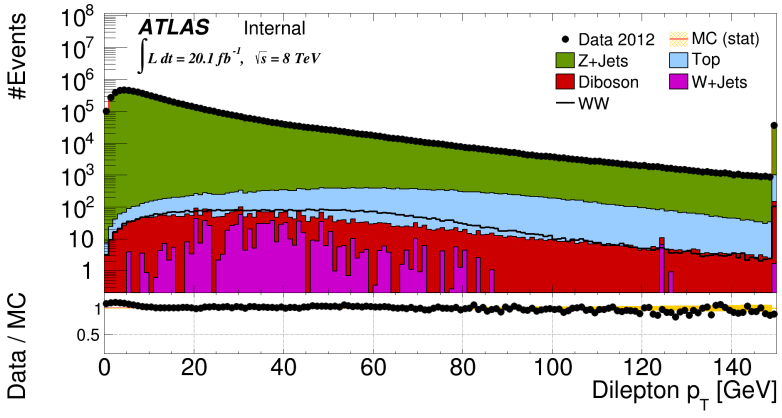

(b) $\mu\mu$ channel

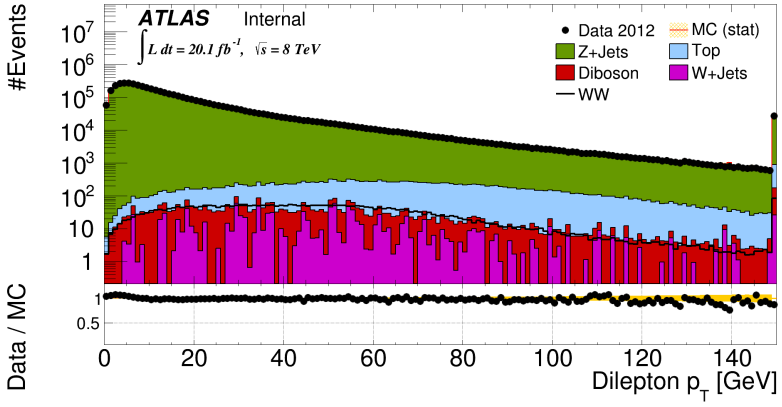

(c) ee channel

Figure 8.3: These plots depict the transverse momentum of the dilepton system after all preselection criteria are applied. On top for $e\mu$ channel, middle $\mu\mu$ channel, and at bottom ee.

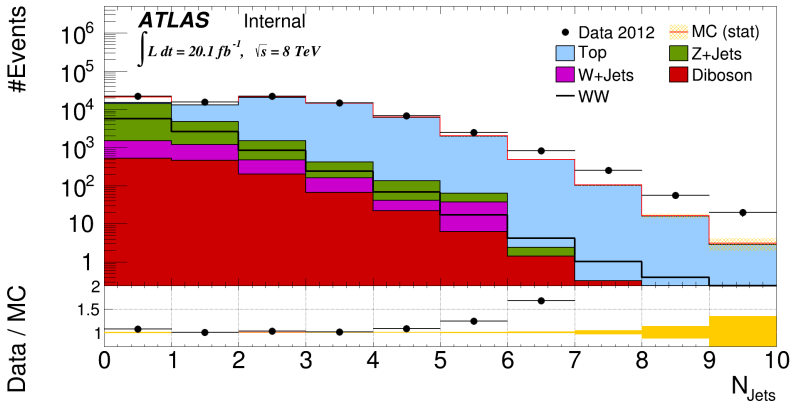

(a) $e\mu$ channel

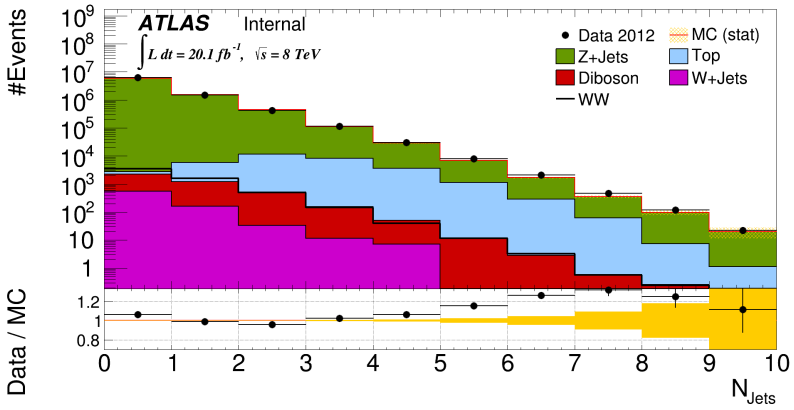

(b) $\mu\mu$ channel

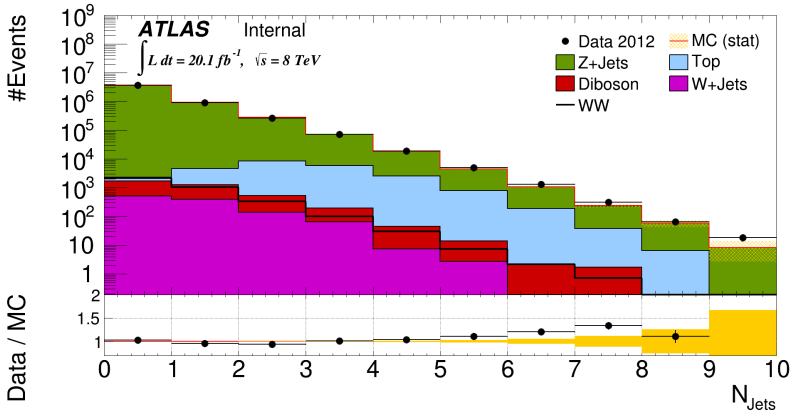

(c) ee channel

Figure 8.4: The jet multiplicity distribution after all preselection criteria are applied. On top for $e\mu$ channel, middle $\mu\mu$ channel, and at bottom ee.

8.2 Event Selection Criteria

The event selection was already explained in section 4.2. A brief summary of the applied selection criteria is given below.

- **Invariant Mass:** The mass of the dilepton system must be greater than 15 GeV for same flavor and greater than 10 GeV for the $e\mu$ channel.
- Z **Veto:** To suppress mainly the decay of the dileptonic decay of the Z boson, the requirement $|M_{l^+l^-} - M_Z| > 15\,\text{GeV}$ is applied in the same flavor channels
- $\not{E}_T^{rel}$**:** $\not{E}_T^{rel} > 45\,\text{GeV}$ for same flavor and $\not{E}_T^{rel} > 25\,\text{GeV}$ in the $e\mu$ channel.
- **Jet Veto:** Every event containing a jet is rejected. The jet object selection is explained in section 5.3. The most important selection criteria for a jet are $p_T > 25\,\text{GeV}$ and $|\eta| > 4.5$.
- **Dilepton Momentum:** $p_{T,ll} > 45\,GeV$ in same flavor and $p_{T,ll} > 25\,\text{GeV}$ in the $e\mu$ channel.

8.2.1 Distributions and Cutflow of Selected Events

This section shows a selection of kinematic distributions in the signal region, after all selection criteria are applied. Figure 8.5 depicts the invariant mass of the leptons $M_{l^+l^-}$ for the different flavor final states. The transverse momenta of the dilepton system p_T^{ll} is shown in figure 8.6. The complete cutflow table is given in table 8.2. The final event yield in the signal region is listed in table 8.3. Similar backgrounds are combined together as already explained in section 8.1.1 for a simpler description.

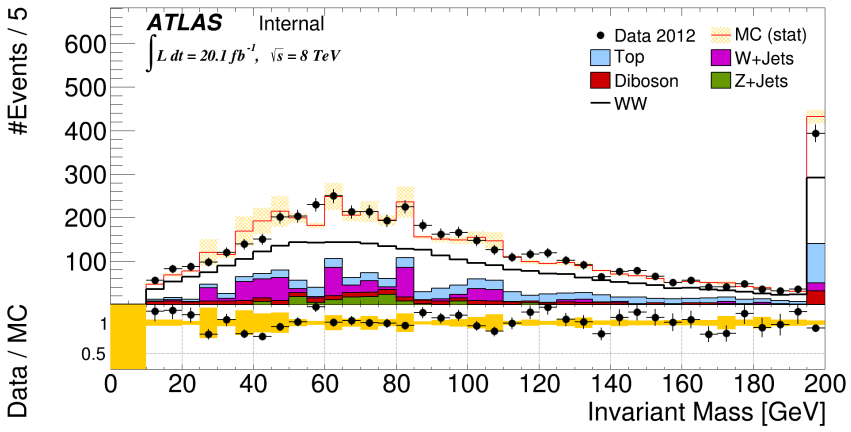

(a) $e\mu$ channel

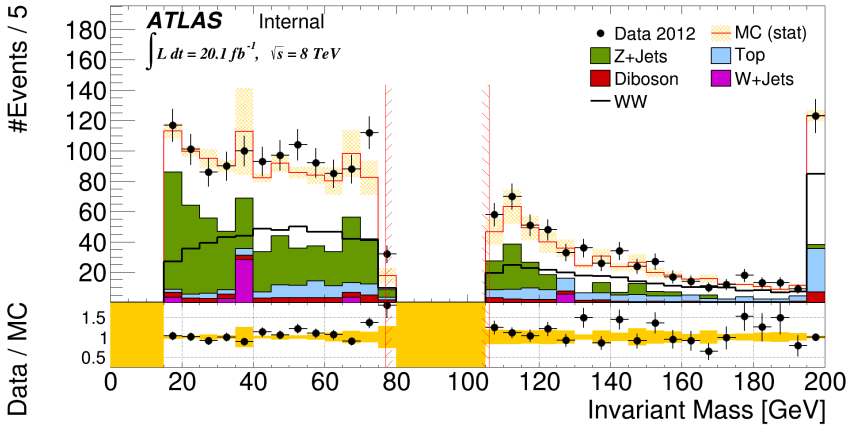

(b) $\mu\mu$ channel

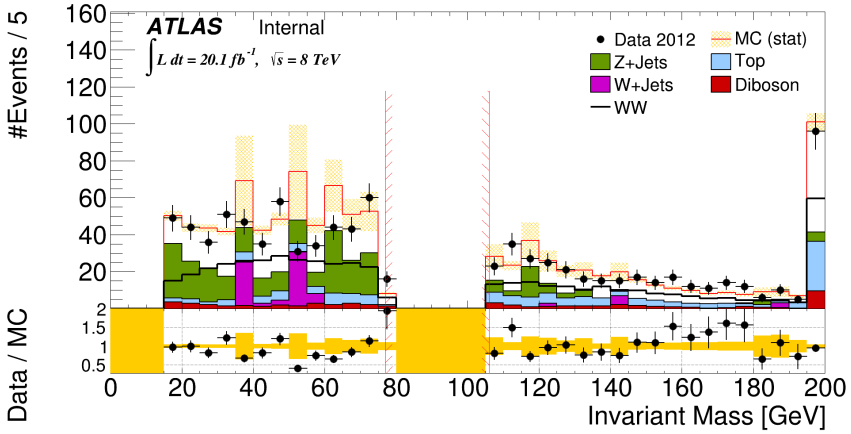

(c) ee channel

Figure 8.5: Distribution of the invariant mass in the signal region.

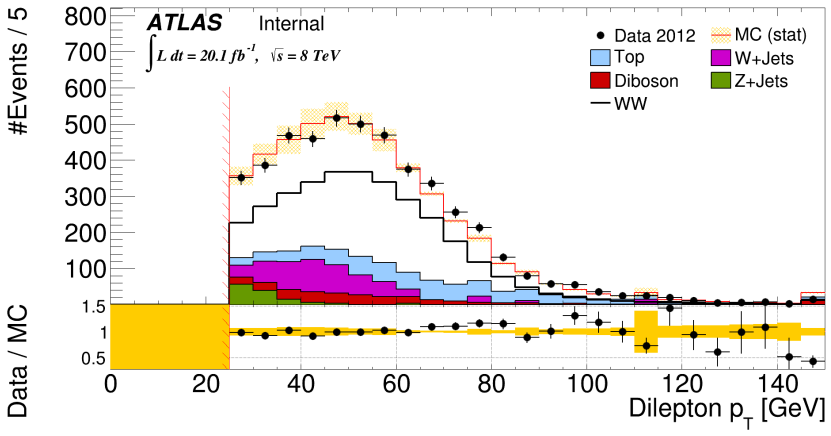

(a) $e\mu$ channel

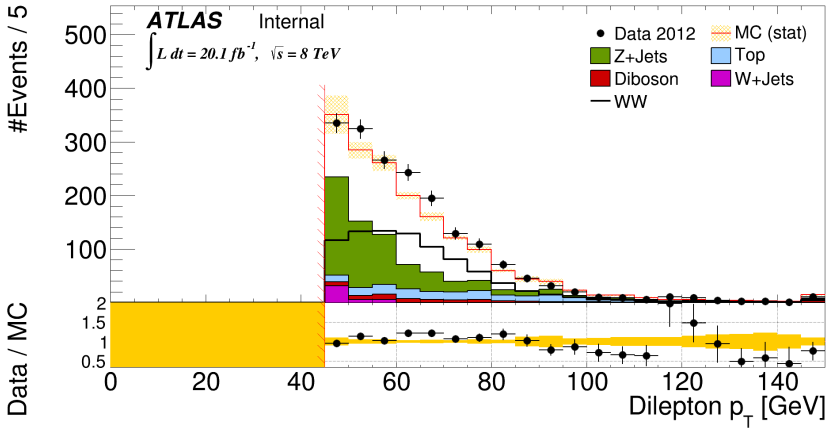

(b) $\mu\mu$ channel

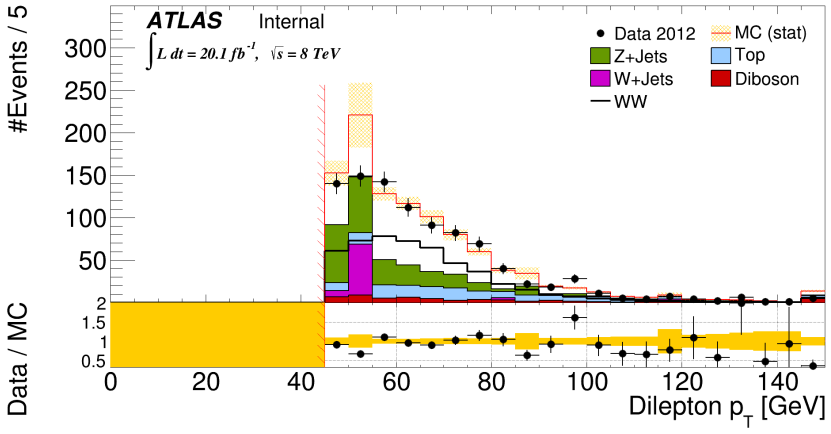

(c) ee channel

Figure 8.6: Distribution of transverse momentum of the dilepton system in the signal region.

$e^{\pm}\mu^{\mp}+\not{E}_T$	Diboson	Top	W+Jets	Z+Jets	W^+W^-	$\frac{S}{\sqrt{S+B}}$	Total MC	Data
Trigger	976660 ± 400	679500 ± 600	213410000 ± 130000	32069000 ± 11000	72176 ± 65	0.55	247210000 ± 130000	525903722
$\not{E}_T$ Cleaning	3555 ± 18	50714 ± 87	3210 ± 240	19180 ± 280	9486 ± 24	19.76	86150 ± 380	90187
2 Leptons	2617 ± 17	50685 ± 87	3210 ± 240	18970 ± 270	9486 ± 24	19.81	84970 ± 380	88760
Opposite Sign	1301 ± 12	50529 ± 87	2160 ± 160	18590 ± 270	9458 ± 24	21.64	82040 ± 330	85679
$p_{T,1} > 25$GeV	1279 ± 12	50409 ± 87	2120 ± 160	17840 ± 270	9413 ± 24	21.98	81070 ± 320	84732
Triggermatch	1272 ± 12	50331 ± 87	2120 ± 160	17680 ± 270	9396 ± 23	21.95	80800 ± 320	84400
$M_{ll} > 10$ GeV	1263 ± 12	50311 ± 87	2120 ± 160	17670 ± 270	9389 ± 23	21.94	80750 ± 320	84346
$\lvert M_Z - M_{ll}\rvert > 15$ GeV	1263 ± 12	50311 ± 87	2120 ± 160	17670 ± 270	9389 ± 23	21.94	80750 ± 320	84346
$\not{E}_T^{rel}$	636.4 ± 8.5	28872 ± 66	1090 ± 110	2384 ± 96	5942 ± 19	23.39	38920 ± 160	39564
Jet Veto	300.3 ± 6.4	668 ± 12	559 ± 94	1638 ± 78	3722 ± 15	25.51	6890 ± 120	6852
$p_{T,ll}$	258.3 ± 6.0	624 ± 12	491 ± 90	123 ± 22	3280 ± 14	28.11	4777 ± 94	4798

$\mu^+\mu^-+\not{E}_T$	Diboson	Top	W+Jets	Z+Jets	W^+W^-	$\frac{S}{\sqrt{S+B}}$	Total MC	Data
Trigger	506320 ± 290	351510 ± 420	108234000 ± 81000	16390100 ± 7900	39494 ± 48	0.48	125521000 ± 82000	221642531
$\not{E}_T$ Cleaning	5060 ± 13	29937 ± 67	910 ± 110	8078100 ± 5600	5912 ± 19	0.94	8119900 ± 5600	8465740
2 Leptons	3916 ± 11	29915 ± 67	910 ± 110	8077900 ± 5600	5912 ± 19	0.94	8118500 ± 5600	8464057
Opposite Sign	3469 ± 10	29890 ± 67	780 ± 100	8077900 ± 5600	5912 ± 19	0.94	8117900 ± 5600	8463023
$p_{T,1} > 25$GeV	3446 ± 10	29753 ± 67	770 ± 100	7991900 ± 5600	5867 ± 19	0.93	8031700 ± 5600	8367259
Triggermatch	3403 ± 10	29398 ± 67	760 ± 100	7930100 ± 5600	5794 ± 18	0.92	7969500 ± 5600	8300818
$M_{ll>15\text{ GeV}}$	3382 ± 10	29218 ± 66	760 ± 100	7919800 ± 5600	5750 ± 18	0.92	7958900 ± 5600	8279624
$\lvert M_Z - M_{ll}\rvert > 15$ GeV	792.1 ± 4.6	22696 ± 59	557 ± 89	621100 ± 1400	4399 ± 16	2.72	649600 ± 1400	692499
$\not{E}_T^{rel}$	175.5 ± 2.6	8385 ± 36	208 ± 56	10660 ± 160	1794 ± 10	7.75	21230 ± 180	20410
Jet Veto	93.8 ± 1.9	208.0 ± 7.2	154 ± 54	7710 ± 140	1142.2 ± 8.1	6.40	9310 ± 150	8558
$p_{T,ll}$	68.6 ± 1.6	176.9 ± 6.6	43 ± 29	565 ± 31	865.4 ± 7.1	14.31	1719 ± 44	1833

$e^+e^-+\not{E}_T$	Diboson	Top	W+Jets	Z+Jets	W^+W^-	$\frac{S}{\sqrt{S+B}}$	Total MC	Data
Trigger	475550 ± 280	378640 ± 440	105210000 ± 100000	15700100 ± 7800	41074 ± 49	0.41	121800000 ± 100000	304425494
$\not{E}_T$ Cleaning	4149 ± 17	20949 ± 56	1930 ± 250	4982800 ± 4400	3774 ± 15	0.76	5013600 ± 4400	5053181
2 Leptons	3388 ± 16	20935 ± 56	1930 ± 250	4982700 ± 4400	3773 ± 15	0.76	5012700 ± 4400	5052137
Opposite Sign	2675 ± 12	20820 ± 56	1130 ± 120	4961200 ± 4400	3750 ± 15	0.76	4989600 ± 4400	5034232
$p_{T,1} > 25$GeV	2672 ± 12	20810 ± 56	1130 ± 120	4955500 ± 4400	3746 ± 15	0.76	4983800 ± 4400	5029884
Triggermatch	2670 ± 12	20806 ± 56	1120 ± 120	4954100 ± 4400	3745 ± 15	0.76	4982400 ± 4400	5028867
$M_{ll} > 15$ GeV	2636 ± 12	20695 ± 56	1120 ± 120	4948400 ± 4400	3718 ± 15	0.75	4976600 ± 4400	5018802
$\lvert M_Z - M_{ll}\rvert > 15$ GeV	839.6 ± 8.6	16182 ± 49	890 ± 110	378100 ± 1100	2856 ± 13	2.25	398900 ± 1100	414072
$\not{E}_T^{rel}$	172.9 ± 4.4	5710 ± 29	195 ± 53	5730 ± 130	1068.1 ± 7.9	5.93	12870 ± 140	11800
Jet Veto	81.0 ± 3.3	158.6 ± 5.9	95 ± 42	4130 ± 110	658.2 ± 6.2	4.71	5120 ± 120	4483
$p_{T,ll}$	58.5 ± 2.8	137.7 ± 5.5	73 ± 36	255 ± 25	505.8 ± 5.4	9.29	1030 ± 44	939

Table 8.2: Full selection cutflow table. The MC is scaled to an integrated luminosity of 20.1 fb^{-1} and the statistical uncertainties are given. On top $e\mu$ channel, middle $\mu\mu$ channel, and bottom ee channel

Background	$e^+e^- + \not{E}_T$	$\mu^+\mu^- + \not{E}_T$	$e^\pm\mu^\mp + \not{E}_T$	Combined
Diboson	58.5 ± 2.8	68.6 ± 1.6	258.3 ± 6.0	385.4 ± 6.8
Top	137.7 ± 5.5	176.9 ± 6.6	624 ± 12	938.6 ± 217.8
W+Jets	73 ± 36	43 ± 29	491 ± 90	607 ± 101.2
Z+Jets	255 ± 25	565 ± 31	123 ± 22	943 ± 45.5
W^+W^-	505.8 ± 5.4	865.4 ± 7.1	3280 ± 14	4651.2 ± 16.6
Total MC	1030 ± 44	1719 ± 44	4777 ± 94	7526 ± 112
Data	939	1833	4798	7570

Table 8.3: Summary of the expected background, predicted signal events, and the observed events. MC events are scaled to an integrated luminosity of $20.1\,\mathrm{fb}^{-1}$.

8.3 Cutflow Comparison Challenge

Although requirements for object definition, event selection criteria, and the same input data sets are fixed, it can happen that different analysis groups get deviating numbers of events after the selections applied, due to the complex analysis structure. It is most important to understand the differences between the analysis groups. The analysis groups collate the number of events in a so-called cutflow comparison challenge. In this procedure the number of events is cross checked after each selection step. Differences between different groups are systematically investigated in order to understand their cause. This is repeated until the groups reach agreement.

For the 2012 data a cutflow comparison challenge was done for six different groups using five different analysis frameworks. The particle identification requirements, as described in chapter 5 are cross checked for electrons, muons, and jets. The preselection requirements, which are described in section 8.1 and the event selection criteria (see section 4.2) are compared as well. In sum, about 40 requirements are cross cross checked between the groups. This analysis uses AOD input files, while the other use n-tuple structured DPD input files called NTUPLE. It can happen that the assigned files for a certain data taking period do not yield exactly the same number of events, e.g. the complex conversion process from the AOD format into the DPD requires a large number of grid jobs and events can be lost due to processing crashes or bookkeeping errors.

The comparison challenge was done on three different subsamples for MC and data. Each sub-sample contain the same number of events in the AOD and NTUPLE input files. This ensures the same initial conditions for the different analysis groups. The contribution of this analysis was to compare and cross-check between AOD and derived data. Several variable calculations in the NTUPLE production process were cross-checked as well.

9 | Cut Optimization Study

In order to suppress the contribution of $Z \to \tau\tau \to e\nu_e\nu_\tau\mu\nu_\mu\nu_\tau$ in the signal region, a cut on M_{ll} can be applied. Figure 9.1 shows the invariant mass distribution after the minimum invariant mass requirement is applied. One can see the peak of $Z \to \tau\tau$ decays around 60 GeV. The implementation of a new selection cut in the $e\mu$ channel is studied.

One important measure for selection cuts is the significance, which is given as

$$\sigma = \frac{S}{\sqrt{S+B}}. \tag{9.1}$$

In this formula S denotes the number of W^+W^- events and B is the sum of all background events.

In addition, the cut optimization is studied applying systematic uncertainty for the jet energy scale. The nominal value of the jet p_T is varied by $\pm 1\sigma$. The uncertainty is given by the difference in event yield from up- and downscaling to the nominal value. The systematic uncertainty of the jet is then taken into account. The corrected significance is given as:

$$\sigma_{\text{sys}} = \frac{S}{\sqrt{S+B+(\Delta B)^2}} \tag{9.2}$$

where ΔB denotes the systematic uncertainty from the energy scale variation. A further important measure is the signal purity, in particular for systematic uncertainties. The purity is defined as the ratio of signal events to background events. Both, significance and purity are calculated after all selection criteria are applied.

The implementation and the variation of the M_{ll} interval is done as follows:

1. M_{ll} **Interval:** The selection interval is implemented with the standard analysis selection. Since the $Z \to \tau\tau$ has a peak at about 60 GeV the lower threshold is varied from 54 GeV to 58 GeV. The upper threshold of the interval is varied from 62 GeV to 66 GeV in 1 GeV steps.

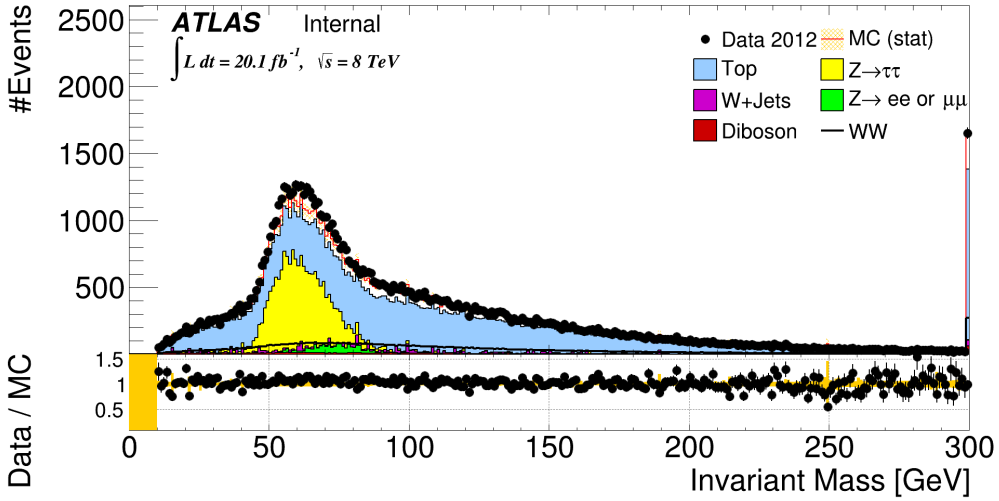

Figure 9.1: The invariant mass of the dileptonic system in the $e\mu$ channel. The contribution of $Z \to \tau\tau \to e\nu_e\nu_\tau\mu\nu_\mu\nu_\tau$ with a peak at about 60 GeV.

2. **Jet Energy Veto:** This analysis rejects all events containing reconstructed jets, and therefore it is sensitive to the jet identification. In the second iteration, the transverse momentum requirement for jets is increased from 25 GeV to 30 GeV and step 1. is repeated.

3. **Missing Energy Selection:** With standard selection requirements, the $\not{E}_T^{rel}$ in the $e\mu$ channel needs to be greater than 25 GeV. This helps to reduce most of the $Z \to \tau\tau$ decays. In the third iteration the $\not{E}_T^{rel}$ requirement is dropped and the steps 1. and 2. are repeated.

4. **Include JES Uncertainty:** The uncertainty for the jet energy scale is taken into account. The points 1. and 2. are repeated and the corrected significance given in equation 9.2 is calculated.

9.1 Significance and Purity Results

In the following subsections the effects on the significance and purity are discussed for steps 1.-4.

9.1.1 M_{ll} Interval and Jet Energy Veto

Figure 9.2 shows the significance and the signal purity as function of the lower and upper M_{ll} cuts. The significance is high for a smaller interval with a maximum of 19.71 for the smallest interval between 58 GeV and 62 GeV. It decreases with a broadened interval to a value of 19.03. The signal purity varies between 73.97% and 74.36%. Compared to the original significance of 20.12, the maximal significance is below the original value. The purity increased for the smallest window from 73.71% to 74.01%.

Figure 9.3 shows the same distribution as Figure 9.2 but the jet energy veto is raised to 30 GeV. The significance increases to a maximum of 19.92 for the smallest Z veto window and decreases to a minimum value of 19.33. No Z veto combination exceeds the original significance of 20.31, while the signal purity is increased for every veto combination. The maximum purity of 67.48% is reached for a Z veto window from 55 GeV to 63 GeV.

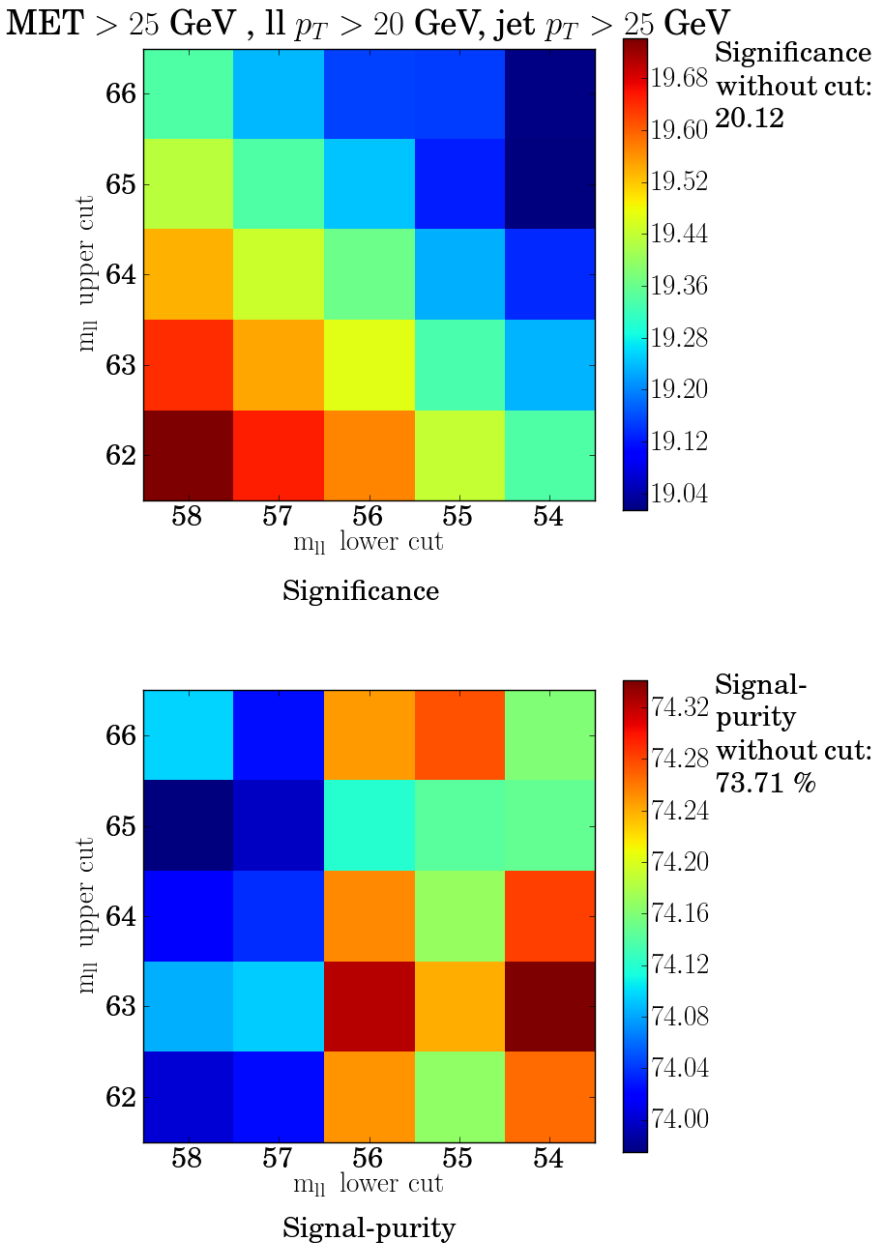

Figure 9.2: The significance on top and the signal purity on the bottom. The interval thresholds of the dileptonic invariant mass are varied.

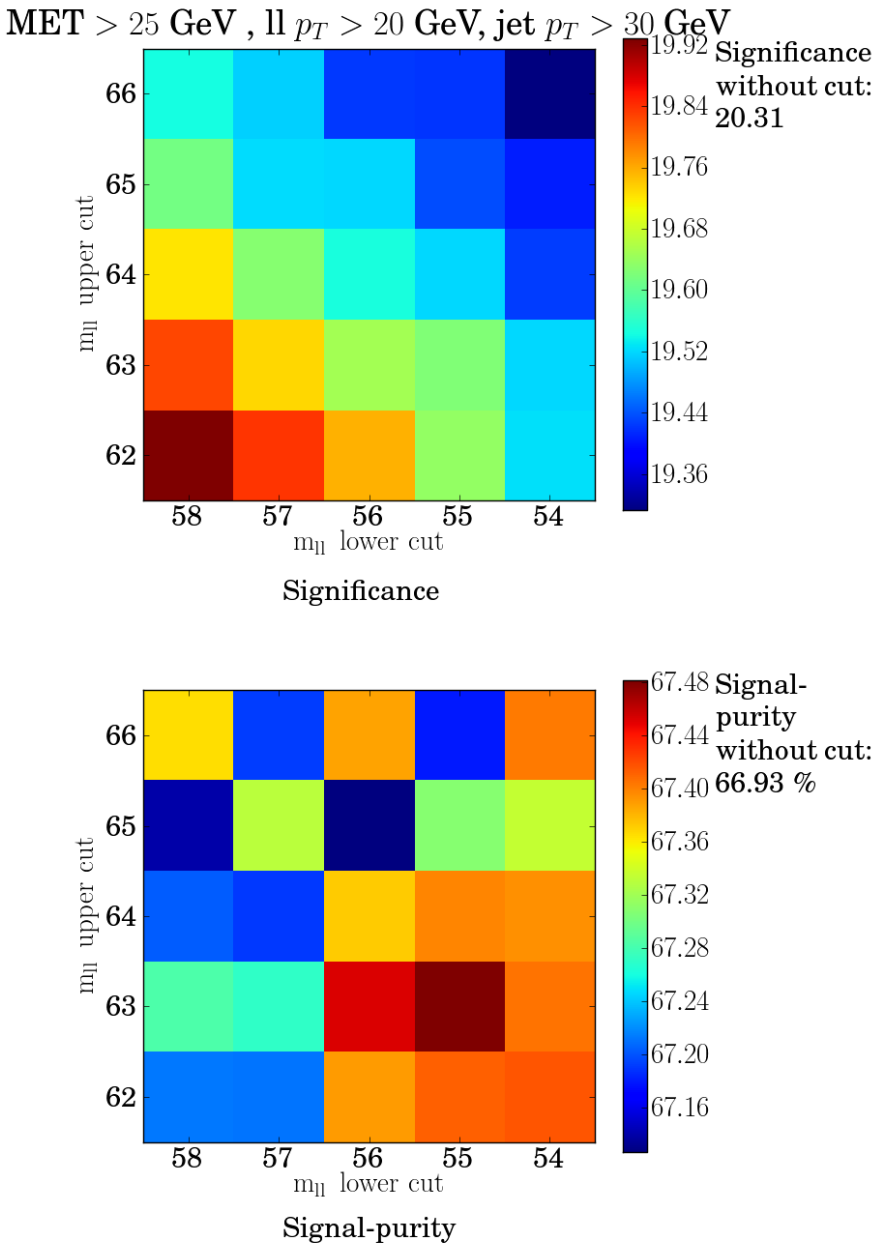

Figure 9.3: Significance (top) and purity (bottom). The jet p_T requirement is increased to 30 GeV.

9.1.2 Missing Transverse Energy Cut

As described under point 3. the $\not{E}_T^{rel}$ requirement is dropped and step 1. and 2. are repeated. Figure 9.4 shows again the significance and the purity. The nominal significance is 20.06. High significance is reached for smaller intervals and it decreases for wider intervals. No combination of lower and upper M_{ll} threshold exceeds the original value of 20.12, which is depicted in figure 9.2. All combinations of the M_{ll} interval exceed the original signal purity of 59.65% by at least 1%. The maximum of 62.77% is reached from 55 GeV to 66 GeV.

Figure 9.5 shows the significance and the purity with the increased requirement on the transverse momentum of the jets. The significance raises with smaller $Z \to \tau\tau$ interval to a maximum of 20.16 at a window from 58 GeV to 62 GeV. The more the interval is broadened, the more the significance decreases. The minimum value for the significance is obtained using the largest M_{ll} of 54 GeV to 66 GeV. The original purity is 53.94% and is exceeded for every interval size. In this case the highest purity is reached for a window of 55 GeV to 66 GeV with a value of 56.91%.

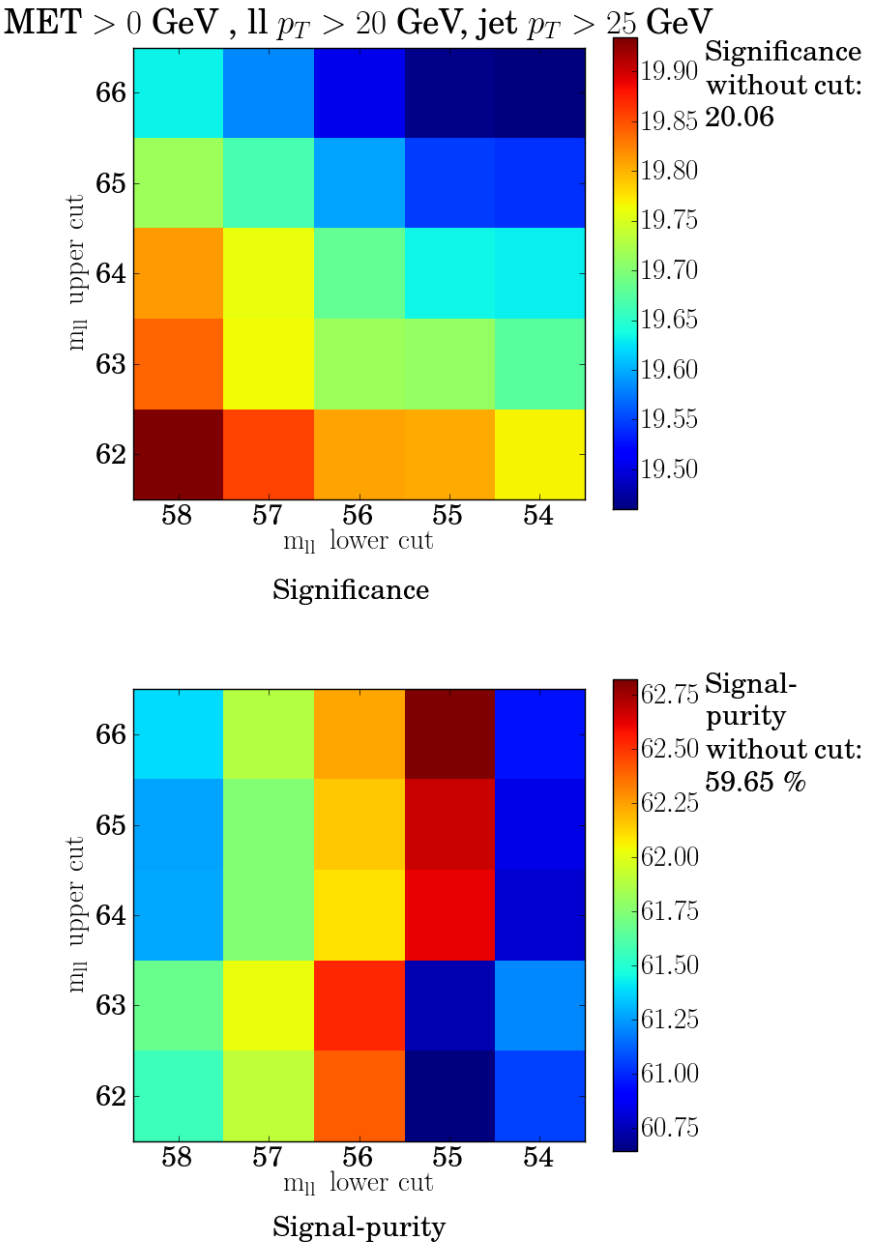

Figure 9.4: The significance on top and the signal purity on the bottom in dependence of the upper and lower $Z \to \tau\tau$. The $\not{E}_T^{rel}$ requirement is dropped.

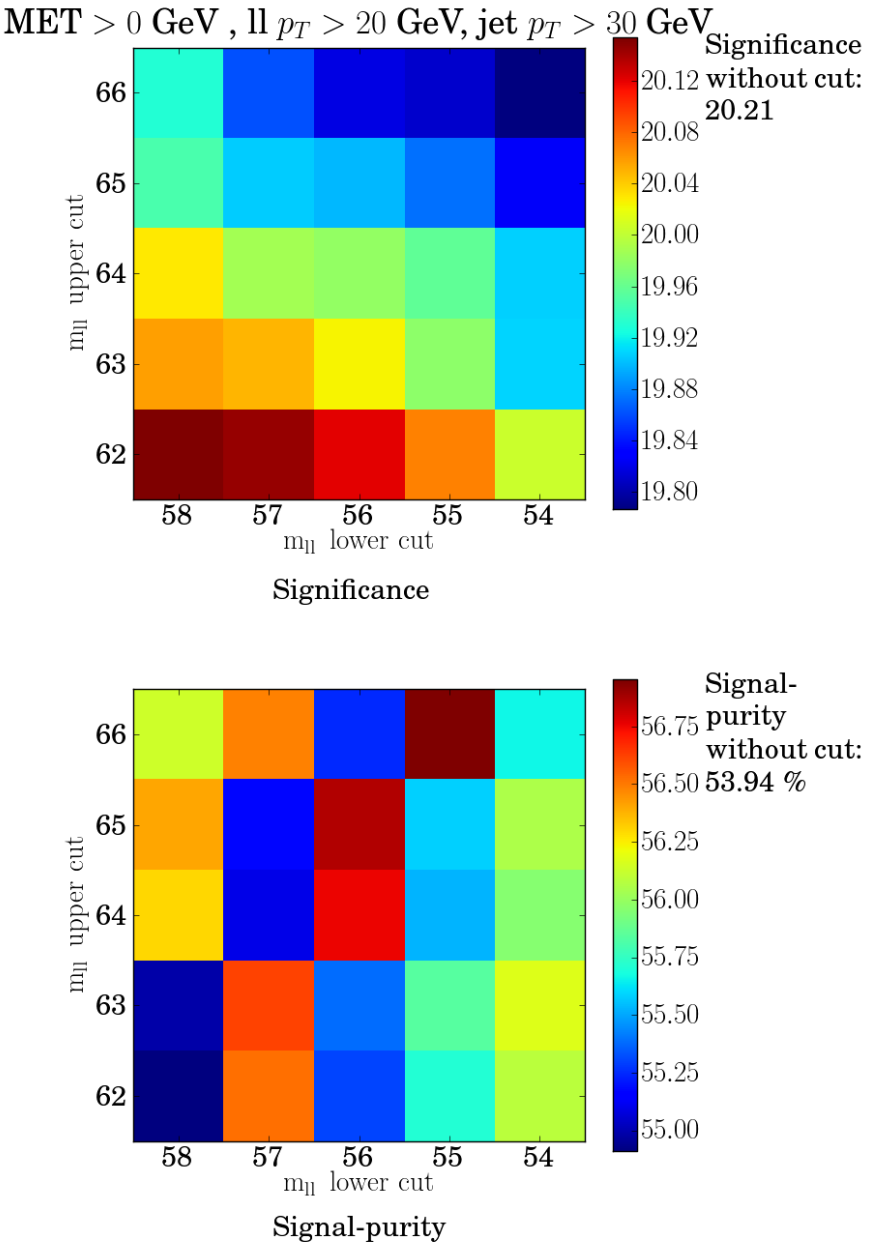

Figure 9.5: The significance on top and the signal purity on the bottom in dependence of the upper and lower $Z \to \tau\tau$ cut. The $\not{E}_T^{rel}$ requirement is dropped and the jet p_T increased to 30 GeV.

9.1.3 Multijet JES Uncertainty

The jet energy scale uncertainty is implemented and the corrected significance given in equation 9.2 is calculated. The procedures described in point 1. and 2. are then repeated. In figure 9.6 the corrected significance and the signal purity are shown. The significance distribution reveals no clear pattern in this study. The maximum value of 9.11 is reached for a veto window from 58 GeV to 65 GeV and exceeds the original corrected significance of 9.04. The maximal purity of 74.36% is reached for an interval from 54 GeV to 63 GeV.

The corrected significance and the purity for the increased jet energy veto is shown in figure 9.7. The nominal significance of 9.76 is greater than the nominal significance shown in figure 9.6. The significance is again higher for smaller intervals and decreases with larger ones. The maximum of 9.68 is given for an interval from 58 GeV to 62 GeV. However, the maximum does not exceed the original corrected significance of 9.76. The purity reaches its maximum for an interval of 55 GeV to 63 GeV with a value of 67.48% and is above the original purity of 66.93%.

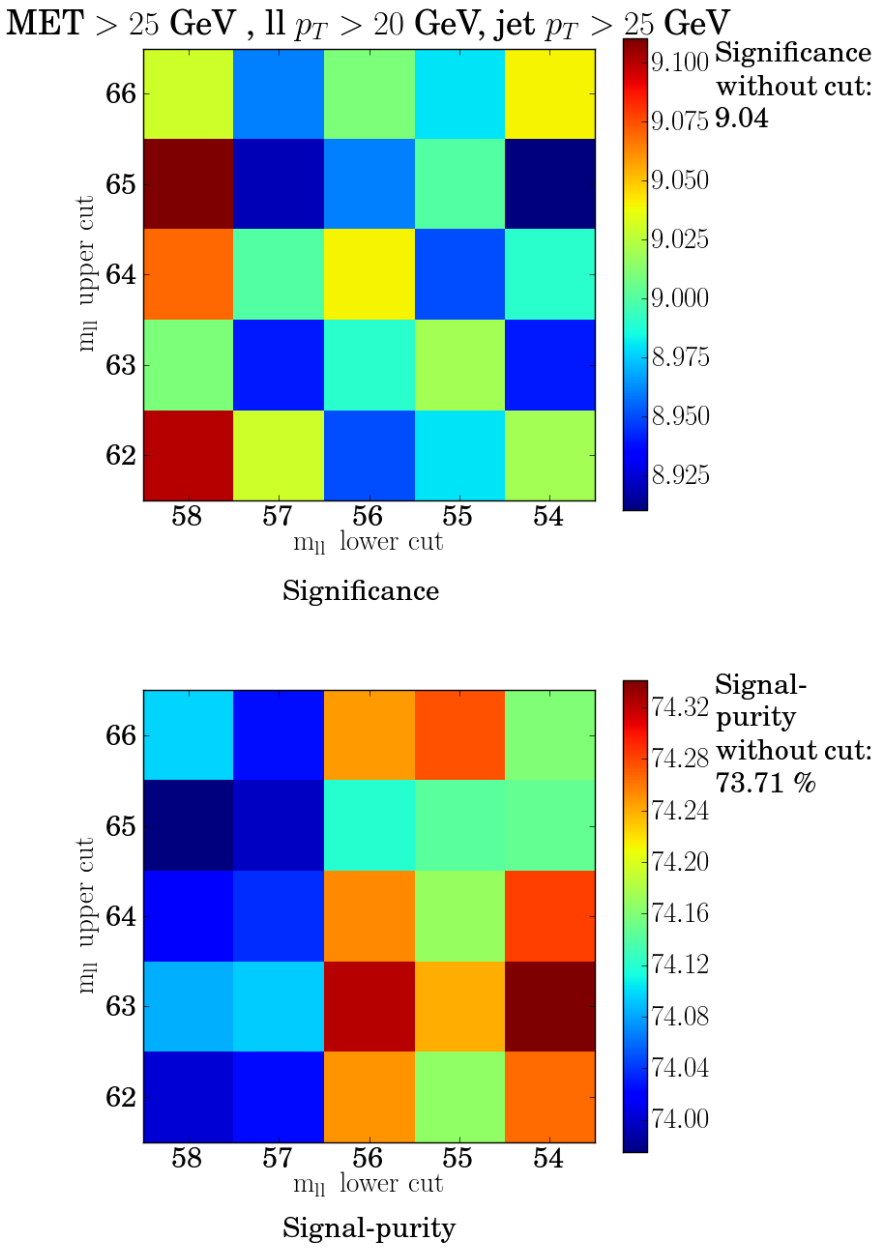

Figure 9.6: The corrected significance on top and the signal purity on the bottom.

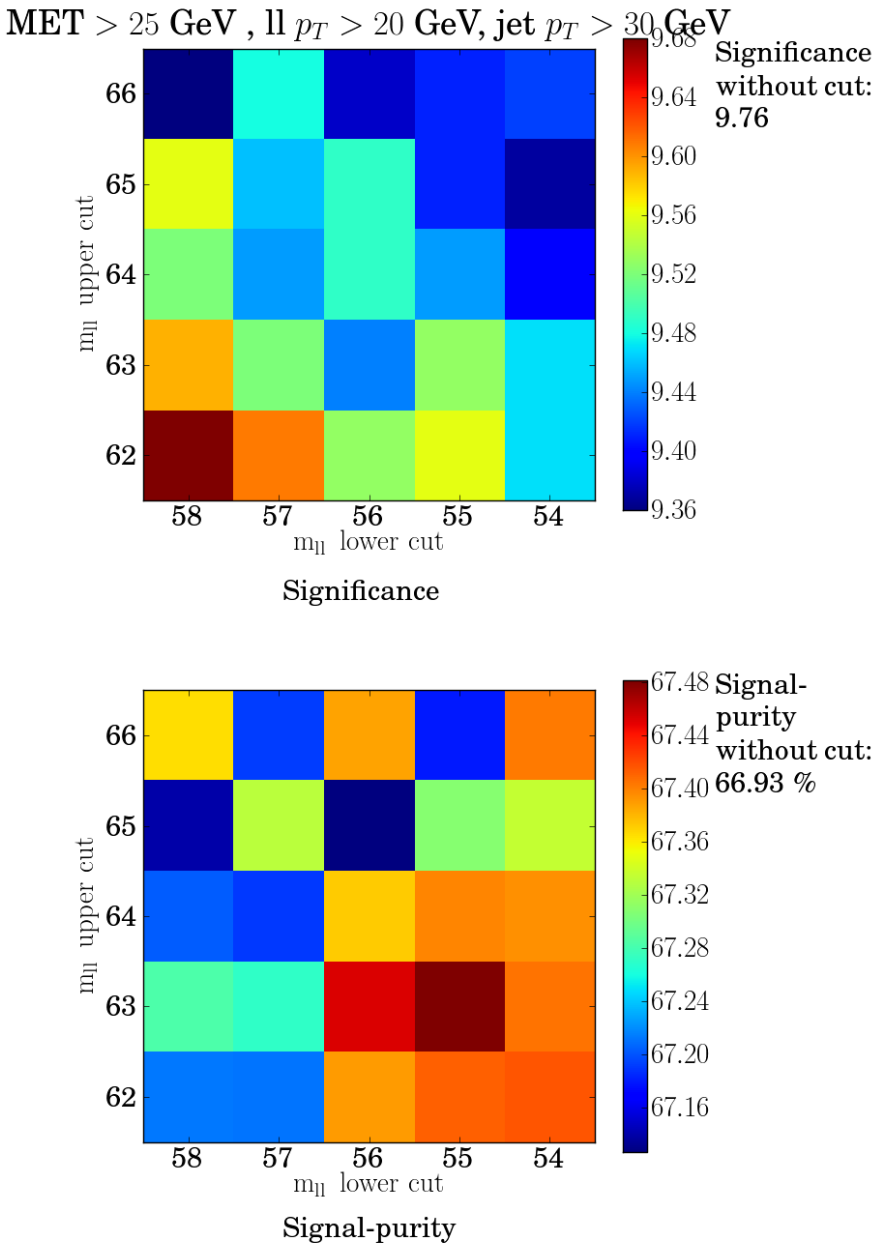

Figure 9.7: The significance on top and the signal purity on the bottom. The jet energy veto is increased to 30 GeV.

9.2 Summary

Section 9.1.1 shows that an implementation of a M_{ll} veto in the $e\mu$ channel does not improve the nominal significance, whereas the purity is increased. A higher threshold for the momentum of the jet with greater than 30 GeV also does not improve the nominal significance. The same combinations of lower and upper bounds for the interval are tested in section 9.1.2 without any requirements on the missing transverse energy. It is found that the purity can be increased but not the significance.

Section 9.1.3 shows the variation of the interval when jet energy scale systematics are taken into account. The significance is increased in comparison to the original for the interval from 58 GeV to 65 GeV, from the original value of 9.04, to 9.11. Increasing the minimum momentum requirement for the jets leads to a distinctly higher significance under consideration of the systematic uncertainty. An implementation of the $Z \rightarrow \tau\tau$ cut in the $e\mu$ channel increases the significance and the signal purity simultaneously when the systemic uncertainty is taken into account. Overall, however, considering the small gains the cut on M_{ll} in the $e\mu$ channel is not applied for the final selection.

10 | Background Estimation

The background modeling done by MC is already very good. However some effects like jets faking leptons are not sufficiently included in these modelings. Therefore data-driven methods are used to acquire proper background descriptions. Background estimation methods for the main backgrounds are briefly described in this section. In addition, the cosmic muon background is estimated.

10.1 W+Jets

This background enters the signal region when a W boson is produced in association with jets. The jet is then misidentified as a lepton and the event has the same signature as the dileptonic decay of a W^+W^- boson pair. Since the description of these jet fake rates is not accurate, the background is estimated with a data-driven fake-factor method.

For the control sample a "jet-rich" lepton is defined. This lepton is enriched in QCD jets. Events in the control region have a well identified lepton and a "jet-rich" lepton. The full analysis object selection criteria are applied, treating the jet as a lepton. The background can then be estimated by scaling the control sample with a fake-factor. The fake-factor f_l is defined for muons and electrons, respectively. It is the ratio of jets passing the full analysis selection criteria to the number of "jet-rich" leptons passing the analysis selections. This fraction is given in equation 10.1. This fake-factor

$$f_l = \frac{N_{\text{identified lepton}}}{N_{\text{jet-rich lepton}}} \tag{10.1}$$

is measured in di-jet events in data. The background estimation is done by scaling the events in the W+Jets control sample, as follows

$$N_{\text{id + fake}} = f_l \times N_{\text{id + jet-rich}}. \tag{10.2}$$

Special for the $e\mu$ channel is that the W+Jets background prediction includes rates from both leptons. The different flavor is taken into account, as given

in equation 10.3.

$$N^{e\mu}_{\text{id }+\text{fake}} = f_e \times N_{\text{id}\,\mu\,+\,\text{jet-rich}\,e} + f_\mu \times N_{\text{id}\,\mu\,+\,\text{jet-rich}\,\mu} \tag{10.3}$$

The definition for the "jet-rich" leptons is similar to the normal lepton selection. Though for the muon the d_0 selection is dropped and the isolation loosened. Only a minimal track requirement is applied for "jet-rich" electrons. The selection of jet enriched fake leptons is done the following way:

- **Trigger:** In the momentum region of $20\,\text{GeV} < p_T < 25\,\text{GeV}$ the trigger EF_g20_etcut is required and the trigger EF_g24_etcut for electrons with p_T greater than 25 GeV. The trigger EF_mu15 is used for muons.
- W **Veto:** Events having a lepton with a higher momentum as 30 GeV are rejected.
- Z **Veto:** In cases where the invariant mass of the leptons is within a 13 GeV region around the Z mass, the event is rejected.
- **EW Subtraction:** Contamination from electroweak processes is subtracted using a WZ inclusive MC simulation.
- **Lepton-Jet Overlap:** If a tight electron overlaps with a jet, the jet is rejected. In case of muons the selection criterion is looser, when overlapping with a jet, the jet is rejected as well.
- $\Delta\phi$ **Muon-Jet:** The difference in the azimuth angle between fake muon and jet must fulfill $\Delta\phi > \pi/2$.

To estimate the systematic uncertainties for this method the cross section of the SM backgrounds are varied. Furthermore systematic uncertainties for the pileup are estimated in dependence of the average number of interactions per bunch crossing. Trigger efficiencies and sample dependence are taken into account as well.

The W+Jets control region contains one loose and one tight lepton. First of all, the tight lepton is required. Afterwards more than one loose lepton is required. Loose leptons with low transverse momentum are removed.

10.2 Z+Jets

The Drell-Yan background ($Z/\gamma* \to l^+l^-$) is the largest background in this analysis. This process contributes to the analysis mostly through mismeasured $\not\!\!E_T$. Since the modeling of the mismeasured $\not\!\!E_T$ is not expected to

be precise in the MC, the contribution of this process as a background is determined by a partially data-driven method.

The scale factor for this is obtained using an control region (CR). The control region is defined by reversing the p_T^{ll} cut in the event selection. The control region is dominated by Z+Jets processes. All other criteria in the event selection remain the same. It is assumed that the discrepancy in the control region between data and MC is caused by the Z+Jets background only. Hence the scale factor is derived as

$$SF = \frac{N_{Z,\mathrm{CR}}^{\mathrm{Data}}}{N_{Z,\mathrm{CR}}^{\mathrm{MC}}} = \frac{N_{\mathrm{CR}}^{\mathrm{Data}} - N_{non-Z,\mathrm{CR}}^{\mathrm{MC}}}{N_{Z,\mathrm{CR}}^{\mathrm{MC}}}. \tag{10.4}$$

In this formula $N_{Z,\mathrm{CR}}^{\mathrm{Data}}$ is the total number of events observed in the control region, $N_{non-Z,\mathrm{CR}}^{\mathrm{MC}}$ is the number of simulated events of non-Z+Jets processes in the control region, and $N_{Z,\mathrm{CR}}^{\mathrm{MC}}$ is the number of simulated events of Z+Jets processes. The derived scale factor is then applied to the predicted MC events in the signal region.

10.3 Top

The preferred decay of the top quark is $t \to Wb$, where the W boson further decays in the leptonic mode. The b quark would result in a jet in the final state, hence most of these top events can be rejected by vetoing on events with jets. However the jet can be misidentified as a second lepton, or since the hadronization of a b quark often results in low energy jets, they can fail the jet selection threshold of $p_T > 25\,\mathrm{GeV}$. Both processes, the top pair $t\bar{t} \to WbWb$ and the single top $tW \to WbW$ contribute to the signal region as a background.

The "Template Method" is also used for the $H \to WW$ analysis and is described in more detail in [61]. This method uses three defined regions. In Signal Region 1 (SR1), the event passes the $\not{E}_T$ selection without the jet veto selection. In Signal Region 2 (SR2) all of the selection criteria are applied. The third region is the Control Region (CR). This is a subset of SR1. The difference is that at least one jet is b-tagged with $p_T > 20\,\mathrm{GeV}$.

The jet multiplicity distribution for SR1 is determined from data by a b-tagged control region. The distribution is extrapolated from the CR to the SR1 using the ratio of SR1 to CR from top MC simulations. The normalized non-top contribution of the CR is fitted to data using a log-likelihood minimization and subtracted from the data in the CR. The estimate in SR1 of top background is then estimated from the 0 jet bin entry. The final estimate in SR2 is done by scaling the data-driven 0 jet bin with the efficiency

of the last cut in respect to the $\not{E}_T^{rel}$ cut. This is also the efficiency of the cut, separating SR1 from SR2.

The statistical uncertainty is calculated from b-tagged CR from data, scaled by the ratio of SR1 and CR of top events from the MC. The systematic uncertainties are estimated by varying the scale and energy resolution of the electron, muon, and jet. In addition the default $\not{E}_T^{rel}$ term is compared with results while the energies of non lepton contributions are varied.

10.4 WZ, ZZ, $W\gamma$, and $W\gamma*$ Diboson Background

The diboson background consists of WZ, ZZ, $W\gamma$, and $W\gamma*$ processes. The estimate for the diboson background is based on MC simulation. The cross sections of these processes are normalized to the integrated luminosity of $20.1\,\mathrm{fb}^{-1}$. The $Z\gamma$ process is already included in the $Z + Jets$ sample used. The estimation for $W\gamma$ is done by using a derived k-factor from comparison of data and simulation [62]. This produces a normalization factor of 1.37 ± 0.10. The given uncertainty results mainly from photon identification uncertainty. Since the virtual photon has low mass, the kinematic distribution for $W\gamma$ and $W\gamma*$ signatures are similar. High mass photon production is included in the WZ samples. In order to avoid double counting of events, the $W\gamma*$ process has an upper limit of 7 GeV and the WZ process samples have a lower limit of 7 GeV on the boson mass. Table 10.1 shows the different boson pairs and their contribution as a background to the event selection channels.

Diboson	e^+e^-	$\mu^+\mu^-$	$e^\pm\mu^\mp$	Combined
ZZ	13.16 ± 0.5	21.13 ± 0.6	4.98 ± 0.2	39.3 ± 0.8
WZ	17.1 ± 1.0	44.6 ± 1.4	112.0 ± 2.3	173.7 ± 2.9
$W\gamma$	10.9 ± 1.4	0.0 ± 0.0	54.6 ± 3.0	65.5 ± 3.3
$W\gamma*$	17.3 ± 2.1	2.9 ± 0.50	86.7 ± 4.6	106.9 ± 5.1
Total	58.5 ± 2.8	68.6 ± 1.6	258.3 ± 6.0	385.4 ± 6.8

Table 10.1: Background estimations for WZ,ZZ,$W\gamma$, and $W\gamma$ and their statistical uncertainties. The numbers are derived from SM simulations, normalized to an integrated luminosity of $20.1\,\mathrm{fb}^{-1}$.

10.5 Cosmic Muons

Pions can be created by cosmic ray protons colliding with particles in the upper atmosphere. The decay fraction of pions to a muon and a muon-neutrino is $\pi^{\pm} \rightarrow \mu^{\pm}\nu_{\mu}$: 99.9% [9]. Due to the time dilation effect of special relativity the μ can survive long enough to reach the earth's surface. This happens with a rate of about 160 Hz per square meter with an energy E_{μ} greater than 1 GeV [34]. High-energy muons, traveling through the ATLAS detector can fire muon triggers. In case the muon travels trough the detector close to an interaction vertex, the muon can be identified as a collision muon. The following section describes two methods for an estimation of the high energy cosmic ray muon.

10.5.1 Cosmic Box

In case the muon travels through the ATLAS detector close to an actual interaction vertex, the muon can be reconstructed as two oppositely charged back-to-back muons, with a small expected $\not{E}_T$. The origin of the two muons is reconstructed in the center of the detector. The muons would appear as back-to-back muons which means their track is a straight line going through the detector. These back-to-back particles can be described by $\Delta\phi = \pi$ and $\eta_1 + \eta_2 = 0$. In order to estimate the rate of this process the detector collected data while no beam collisions took place. The data taken in 2011 shows that 99.7% of the cosmic muons are within a region of $\Delta\phi - \pi < 0.0015$ and $|\eta_1 + \eta_2| < 0.002$. The contribution as a background is determined by counting muons, which pass the normal lepton analysis selection, in the box of $\Delta\phi - \pi < 0.0015$ and $|\eta_1 + \eta_2| < 0.002$. There are not exclusively cosmic muons in this box, but also muons from collision events. The muons from collisions are estimated from a broadened region of $|\eta_1 + \eta_2| < 0.006$ and $|\Delta\phi - \pi| < 0.0045$. The broadened box can be divided into nine areas with the same size of the cosmic box.

Excluding the actual cosmic box, the eight boxes left of the broadened region contain 204 events in total, 13 passing the Z veto. The extrapolated collision events for a box of the original size is 25.5 ± 5.0 on total and 1.6 ± 1.3 reaching the Z veto. For the 2012 LHC data 40 events are observed in the cosmic box. Only 15 passed the Z mass cut. Each of those 15 events failed the missing E_T cut. These numbers indicate that the cosmic background is negligible. The distribution of these events is depicted in figure 10.1.

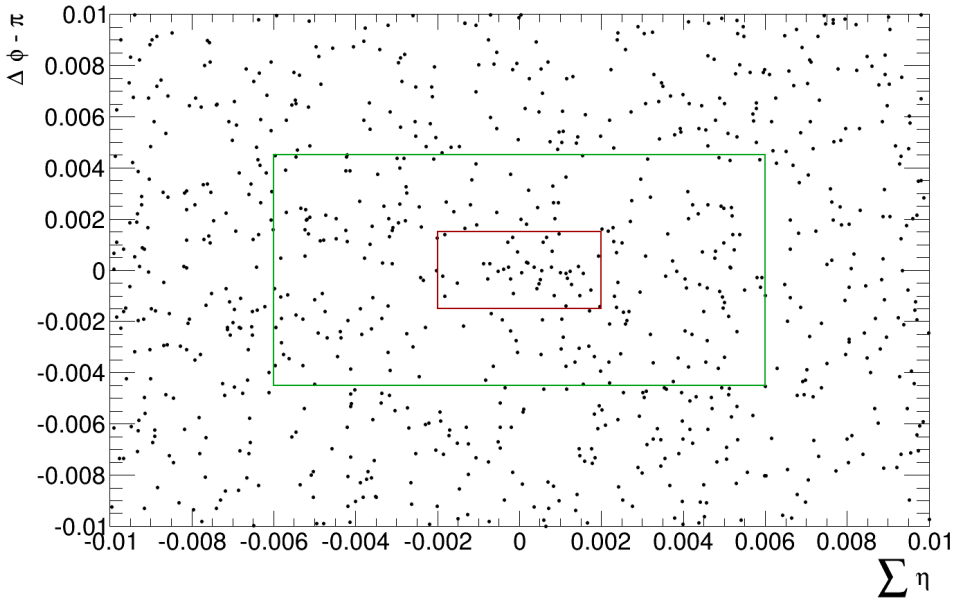

Figure 10.1: The distribution of the dilepton system in the $\eta - \phi$ plane. The red box indicates the cosmic box, in which 99.7% of cosmic muons are in. The green box indicates the broadened box, with which the background for the red box is estimated. The data used corresponds to an integrated luminosity of $20.1\,\mathrm{fb}^{-1}$.

10.5.2 Lower Half Track

A second possibility how cosmic ray muons can contribute to the WW selection is when only the lower half of the muon is tracked. This happens when the upper half of the track is outside of the triggering window of the detector. In case where an electron or muon is already produced from collisions, the signature looks like the dileptonic decay of W^+W^-. To estimate the contribution of these events the primary vertex-track requirement is dropped and lepton impact parameter (d_0 and Δz_0) cuts are loosened. The events in the region of $20\,\mathrm{mm} < \Delta z_0 < 120\,\mathrm{mm}$ are counted and linearly extrapolated to the interesting region of $\Delta z_0 = 1\,\mathrm{mm}$.

Due to the loosened impact parameter requirements of the muon this also contains leptons produced in pileup collisions, which is constrained as well this way. The control region of Δz_0 between 20 mm and 120 mm, which is depicted in figure 10.3 for the $\mu\mu$ channel, encloses 133 events. Extrapolated to the the region of 1 mm one can expect about 1.3 cosmic muons (or pileup)

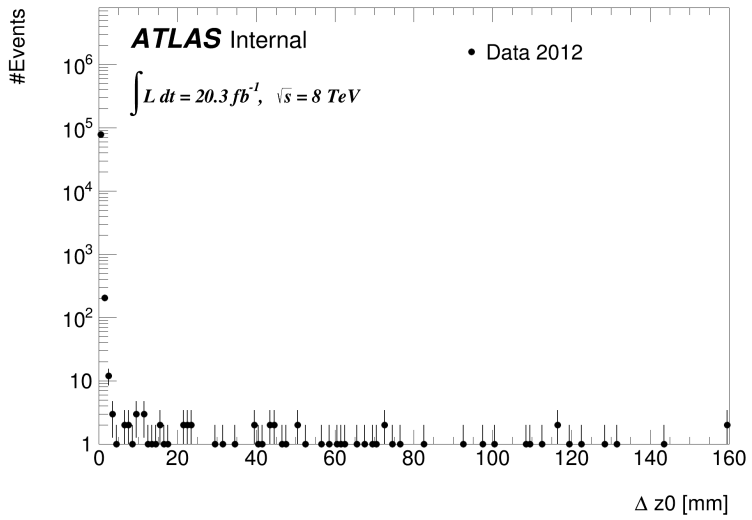

Figure 10.2: $\Delta z_0(\mu, l)$ after regular preselection in the cosmic control region for $e\mu$ channel with loosened vertex cuts. The control region is in the range $20\,\text{mm} < \Delta\text{z}_0(\mu, \text{l}) < 120\,\text{mm}$ and encloses 45 events.

passing the preselection cuts. The control region for the $e\mu$ channel contains 45 Events, extrapolated to 1 mm one can expect less than 0.5 cosmic muons (or pileup). The control region is shown in figure 10.2.

In consideration of loosened impact parameters and vertex requirements during the estimation, the amount of cosmic muons is substantially further reduced when the normal event selection is applied. Therefore this type of cosmic background can be neglected as well.

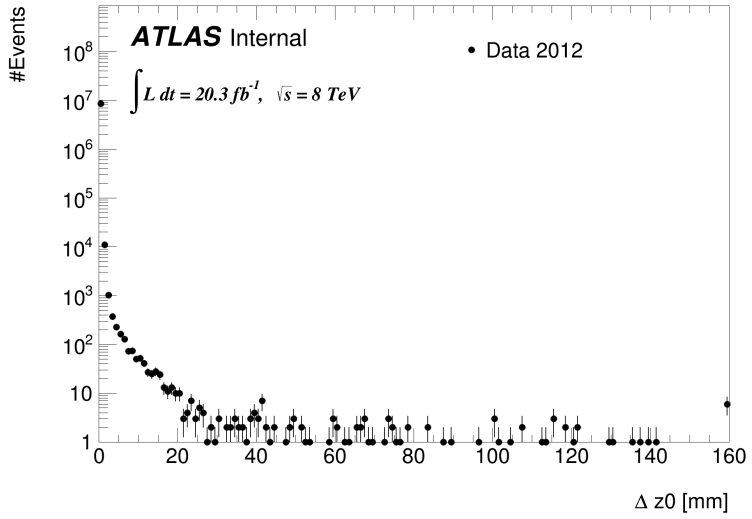

Figure 10.3: $\Delta z_0(\mu, l)$ after regular preselection in the cosmic control region for $\mu\mu$ channel with loosened vertex cuts. The control region is in the range $20\,\mathrm{mm} < \Delta \mathrm{z}_0(\mu, \mathrm{l}) < 120\,\mathrm{mm}$ and encloses 133 events.

11 | Summary and Outlook

This thesis studied the production of W^+W^- boson pair with the ATLAS detector at a center-of-mass energy of $\sqrt{8}\,\text{TeV}$. The analysis is based on a study of 2011 data, which has been updated to match the demands of the data recorded during the year 2012. The analysis was cross checked with six different analysis groups from the ATLAS collaboration. More than 40 parameters were compared in a cut-flow challenge. New calibration scales and corrections were implemented. The contribution of $Z \to \tau\tau$ decays in the $e\mu$ channel has been studied and improvements have been investigated in a cut optimization study. A $Z \to \tau\tau$ veto based on a invariant mass interval around the decay peak of the Z boson has been implemented and the effects on significance and signal purity have been investigated. Improvements could be obtained but they were considered too small to warrant a change of the established selection criteria. However, it was shown that systematic uncertainties can have a significant impact on cut optimization and should be taken into account. For an update of the measurement of the W^+W^- production cross section in proton-proton collisions at the LHC with the ATLAS detector, the cosmic muon background has been estimated. Cosmic muons can be falsely reconstructed as muons from a proton-proton interaction in the ATLAS detector. Based on analysis of cosmic data it was found that the event and particle selection criteria do sufficiently suppress the contribution of the cosmic muons.

The final determination of the W^+W^- cross section production at the LHC with 2012 data is still in progress. It is crucial to implement data driven methods for background estimations and to estimate the systematic uncertainties on which other analysis groups are still working. A conference contribution containing the final ATLAS result with contributions from this thesis is in preparation.

Bibliography

[1] P. W. Higgs, Broken symmetries and the masses of gauge bosons, *Phys.Rev.Lett.* **13**, 508–509 (1964).

[2] The ATLAS Collaboration, Observation of a new particle in the search for the Standard Model Higgs boson with the ATLAS detector at the LHC, Phys.Lett. B716 (2012) 1-29, 2012.

[3] S. Chatrchyan et al., Observation of a new boson at a mass of 125 GeV with the CMS experiment at the LHC, *Phys.Lett.* **B716**, 30–61 (2012), 1207.7235.

[4] Cern press office, New results indicate thtat particle discovered at CERN is a Higgs boson.

[5] Fermilab Pressrelease, Discoveries at Fermilab - Discovery of the Bottom Quark.

[6] F. Abe et al., Observation of top quark production in $\bar{p}p$ collisions, *Phys.Rev.Lett.* **74**, 2626–2631 (1995), hep-ex/9503002.

[7] D. Griffiths, *Introduction to Elementary Particles*, Physics Textbook, Wiley, 2008.

[8] Combined measurements of the mass and signal strength of the Higgs-like boson with the ATLAS detector using up to 25 fb^{-1} of proton-proton collision data, Technical Report ATLAS-CONF-2013-014, CERN, Geneva, Mar 2013.

[9] J. Beringer et al., Review of Particle Physics (RPP), *Phys.Rev.* **D86**, 010001 (2012).

[10] G. Sterman, *An Introduction To Quantum Field Theory*, Physics Textbook, Cambridge University Press, 1993.

[11] F. Halzen and A. Martin, *Quarks and leptons: an introductory course in modern particle physics*, Wiley, 1984.

[12] G. Guralnik, C. Hagen, and T. Kibble, Global Conservation Laws and Massless Particles, *Phys.Rev.Lett.* **13**, 585–587 (1964).

[13] F. Englert and R. Brout, Broken symmetries and the masses of guage vector mesons, *Phys.Rev.Lett.* **13**, 321–323 (1964).

[14] I. C. Brock, Higgs potential.

[15] C. Berger, *Elementarteilchenphysik*, Physics Textbook, Springer, 2006.

[16] J. M. Campbell, R. K. Ellis, and C. Williams, Vector boson pair production at the LHC, *JHEP* **1107**, 018 (2011), 1105.0020.

[17] E. Benedikt, M., E. Collier, P., E. Mertens, V., E. Poole, J., and E. Schindl, K., LHC Design Report. 3. The LHC injector chain, (2004).

[18] Atlas Collaboration, Luminosity Public Results, https://twiki.cern.ch/twiki/bin/view/AtlasPublic/LuminosityPublicResults.

[19] C. Lefèvre, The CERN accelerator complex. Complexe des accélérateurs du CERN, Dec 2008.

[20] CERN, Brochure 2009, 2009.

[21] J. Pequenao, Computer generated image of the whole ATLAS detector, Mar 2008.

[22] M. Lamprecht, Studien zu Effizienz und Akzeptanz des ATLAS-Myontriggers mit simulierten Messdaten, (2007).

[23] ATLAS: Detector and physics performance technical design report. Volume 1, (1999).

[24] ATLAS inner detector: Technical design report. Vol. 1, (1997).

[25] G. Aad et al., Readiness of the ATLAS Liquid Argon Calorimeter for LHC Collisions, *Eur.Phys.J.* **C70**, 723–753 (2010), 0912.2642.

[26] G. Aad et al., Readiness of the ATLAS Tile Calorimeter for LHC collisions, *Eur.Phys.J.* **C70**, 1193–1236 (2010), 1007.5423.

[27] J. Pequenao, Computer generated image of the ATLAS Muons subsystem, Mar 2008.

[28] Duckeck, G., (Ed.) and others, ATLAS computing: Technical design report, (2005).

[29] Cern.ch, The Grid: A system of tiers, https://home.web.cern.ch/about/computing/grid-system-tiers.

[30] Measurement of the W^+W^- Production Cross Section in Proton-Proton Collisions at $\sqrt{s} = 7$ TeV with the ATLAS Detector, (ATLAS-CONF-2012-025) (Mar 2012).

[31] A Combination of preliminary electroweak measurements and constraints on the standard model, (2005), hep-ex/0511027.

[32] V. Abazov et al., Measurement of the WW production cross section with dilepton final states in p anti-p collisions at $\sqrt{s} = 1.96$-TeV and limits on anomalous trilinear gauge couplings, *Phys.Rev.Lett.* **103**, 191801 (2009), 0904.0673.

[33] T. Aaltonen et al., Measurement of the W^+W^- Production Cross Section and Search for Anomalous WW gamma and WWZ Couplings in p p-bar Collisions at $\sqrt{s} = 1.96$-TeV, *Phys.Rev.Lett.* **104**, 201801 (2010), 0912.4500.

[34] J. Ebke, Measurement of the W^+W^- diboson production cross-section with the ATLAS Experiment at the Large Hadron Collider, (2011).

[35] Measurement of WW production rate, (2012).

[36] S. Chatrchyan et al., Measurement of WW and ZZ production cross sections in pp collisions at $\sqrt{s} = 8$ TeV, *Phys. Lett. B* **721**(arXiv:1301.4698. CMS-SMP-12-024. CERN-PH-EP-2012-376), 190–211 (Jan 2013).

[37] Expected electron performance in the ATLAS experiment, (2011).

[38] G. Aad et al., Electron performance measurements with the ATLAS detector using the 2010 LHC proton-proton collision data, *Eur.Phys.J.* **C72**, 1909 (2012), 1110.3174.

[39] B. Resende, Muon identification algorithms in ATLAS, *PoS* **EPS-HEP2009**, 431 (2009).

[40] M. Cacciari, G. P. Salam, and G. Soyez, The Anti-k(t) jet clustering algorithm, *JHEP* **0804**, 063 (2008), 0802.1189.

[41] P. Schieferdecker, Jet Algorithms, (2009).

[42] Atlas Collaboration, Jet Guidelines for Analyses of 2012 Data, *Interal Documentation, revision* **r31**, https://twiki.cern.ch/twiki/bin/viewauth/AtlasProtected/JetStudies2012.

[43] Atlas Collaboration, Jet Vertex Fraction, *Interal Documentation, revision* **r32**, https://twiki.cern.ch/twiki/bin/view/AtlasProtected/JetVertexFraction.

[44] M. Dobbs, S. Frixione, E. Laenen, K. Tollefson, H. Baer, et al., Les Houches guidebook to Monte Carlo generators for hadron collider physics, pages 411–459 (2004), hep-ph/0403045.

[45] Agostinelli, S. et al., Geant 4 - A Simulation toolkit, page 250 (2003).

[46] J. M. Campbell, R. K. Ellis, P. Nason, and G. Zanderighi, W and Z bosons in association with two jets using the POWHEG method, (2013), 1303.5447.

[47] S. Alioli, POWHEG: Status and perspectives, *PoS* **EPS-HEP2011**, 280 (2011).

[48] T. Sjostrand, S. Mrenna, and P. Z. Skands, A Brief Introduction to PYTHIA 8.1, *Comput.Phys.Commun.* **178**, 852–867 (2008), 0710.3820.

[49] T. Binoth, M. Ciccolini, N. Kauer, and M. Kramer, Gluon-induced W-boson pair production at the LHC, *JHEP* **0612**, 046 (2006), hep-ph/0611170.

[50] P. Lenzi, AlpGen and SHERPA in Z/gamma* + jets at LHC, pages 740–746 (2009).

[51] S. Frixione and B. R. Webber, Matching NLO QCD computations and parton shower simulations, *JHEP* **0206**, 029 (2002), hep-ph/0204244.

[52] R. C. Gray, C. Kilic, M. Park, S. Somalwar, and S. Thomas, Backgrounds To Higgs Boson Searches from Wgamma* - lvlv, Asymmetric Internal Conversion, (2011), 1110.1368.

[53] Atlas Collaboration, Pileupreweighting, *Interal Documentation, revision* **r23**, https://twiki.cern.ch/twiki/bin/view/AtlasProtected/PileupReweighting.

[54] Atlas Collaboration, Electron Gamma Efficiency Measurements 2012, https://twiki.cern.ch/twiki/bin/viewauth/AtlasProtected/EfficiencyMeasurements2012.

[55] Atlas Collaboration, Egamma Guidelines for Analyses of 2012 Data, *Interal Documentation, revision* **r22**, https://twiki.cern.ch/twiki/bin/viewauth/AtlasProtected/Egamma2012Analyses.

[56] Atlas Collaboration, Preliminary Guidelines for Analyses of 2012 Data, *Interal Documentation, revision* **r56**, https://twiki.cern.ch/twiki/bin/viewauth/AtlasProtected/MCPAnalysisGuidelinesData2012.

[57] Mateos, D. L. and Gillberg, D., Plans and technicalities for 2012 JES analyses, Jet calibration and resolution, 2012.

[58] Atlas Collaboration, Summer 2012 Reprocessing, *Interal Documentation, revision* **r163**, https://twiki.cern.ch/twiki/bin/viewauth/Atlas/Summer2012Reprocessing.

[59] Atlas Collaboration, Data Preparation Checklist for Physics Analysis, *Interal Documentation, revision* **r13**, https://twiki.cern.ch/twiki/bin/viewauth/Atlas/DataPreparationCheckListForPhysicsAnalysis.

[60] Atlas Collaboration, Recommendations for jet cleaning for data 2012, *Interal Documentation, revision* **r11**, https://twiki.cern.ch/twiki/bin/viewauth/AtlasProtected/HowToCleanJets2012.

[61] A. Belloni, G. Conti, J. Guimaraes da Costa, J. Huth, and C. Mills, Top Background Estimation Using Jet Multiplicity Distributions, ATL-COM-PHYS-2012-856, June 2012.

[62] G. Aad et al., Measurement of W gamma and Z gamma production cross sections in pp collisions at $\sqrt{s} = 7$ TeV and limits on anomalous triple gauge couplings with the ATLAS detector, (2012), 1205.2531.

Acknowledgements

Ich möchte mich bei folgenden Personen bedanken:

- Prof. Dr. Dorothee Schaile für die Aufnahme an ihrem Lehrstuhl und die Möglichkeit in der ATLAS Kollaboration arbeiten zu dürfen.
- Dr. Günter Duckeck und Dr. Johannes Ebke für die herausragende Betreung während meiner Arbeit am Lehrstuhl.
- Allen weiteren Mitgliedern des Lehrstuhls für ein sehr angenehmes Arbeitsklima.
- Meiner Mutter, Ursula Rättich und in Erinnerung an meinen Vater, Helmut Rättich, sowie meinen Geschwistern Susanne, Carolin, Anja und Barbara für die ununterbrochene Unterstüzung.
- Meinen Freunden Martin Reitter, Arvid Kingel, und dem Spezi-Team: Friedrich Hönig und Philipp Heimpel für eine sehr lustige und schöne Zeit während des Studiums.
- Allen meinen Freunden mit denen ich sehr viel Erlebt hab und auch weiterhin werde.

Erklärung

Hiermit erkläre ich, die vorliegende Arbeit selbständig verfasst zu haben und keine anderen als die in der Arbeit angegebenen Quellen und Hilfsmittel benutzt zu haben.

München, den 27.4.2013

_____

(Florian Rättich)